Secondary magnetite in ancient zircon precludes analysis of a Hadean geodynamo

Fengzai Tang[a], Richard J. M. Taylor[a,1], Josh F. Einsle[a,b], Cauê S. Borlina[c], Roger R. Fu[d], Benjamin P. Weiss[c], Helen M. Williams[a], Wyn Williams[e], Lesleis Nagy[f], Paul A. Midgley[b], Eduardo A. Lima[c], Elizabeth A. Bell[g], T. Mark Harrison[g], Ellen W. Alexander[g], and Richard J. Harrison[a]

[a]Department of Earth Sciences, University of Cambridge, CB2 3EQ Cambridge, United Kingdom; [b]Department of Materials Science and Metallurgy, University of Cambridge, CB2 3EQ Cambridge, United Kingdom; [c]Department of Earth, Atmospheric, and Planetary Sciences, Massachusetts Institute of Technology, Cambridge, MA 02139; [d]Department of Earth and Planetary Sciences, Harvard University, Cambridge, MA 02138; [e]School of Geosciences, University of Edinburgh, EH9 3FE Edinburgh, United Kingdom; [f]Geoscience Research Division, University of California, San Diego, La Jolla, CA 92093; and [g]Department of Earth, Planetary, and Space Sciences, University of California, Los Angeles, CA 90095

Edited by Donald J. DePaolo, Lawrence Berkeley National Laboratory, Berkeley, CA, and approved November 27, 2018 (received for review June 28, 2018)

Zircon crystals from the Jack Hills, Western Australia, are one of the few surviving mineralogical records of Earth's first 500 million years and have been proposed to contain a paleomagnetic record of the Hadean geodynamo. A prerequisite for the preservation of Hadean magnetization is the presence of primary magnetic inclusions within pristine igneous zircon. To date no images of the magnetic recorders within ancient zircon have been presented. Here we use high-resolution transmission electron microscopy to demonstrate that all observed inclusions are secondary features formed via two distinct mechanisms. Magnetite is produced via a pipe-diffusion mechanism whereby iron diffuses into radiation-damaged zircon along the cores of dislocations and is precipitated inside nanopores and also during low-temperature recrystallization of radiation-damaged zircon in the presence of an aqueous fluid. Although these magnetites can be recognized as secondary using transmission electron microscopy, they otherwise occur in regions that are indistinguishable from pristine igneous zircon and carry remanent magnetization that postdates the crystallization age by at least several hundred million years. Without microscopic evidence ruling out secondary magnetite, the paleomagnetic case for a Hadean–Eoarchean geodynamo cannot yet been made.

Hadean | paleomagnetism | Jack Hills | zircon | correlative microscopy

The earliest paleomagnetic evidence for an active geodynamo comes from circa (c.) 3.45-billion-year-old (Ga) rocks from the Barberton Greenstone Belt and the Pilbara Craton (1–3). According to many core formation models, the fields recorded by these rocks predate inner-core solidification, the process that powers the present-day geodynamo through the release of light elements at the inner-core/outer-core boundary. Before inner-core solidification, the geodynamo may have been powered by thermal convection alone. Recent upward revision of core thermal conductivity (4–6) means that high heat flux is needed to meet paleomagnetic constraints for a pure thermal dynamo. This leads to surprising predictions of a very young inner core (<600 Ma) and initial core temperatures that were hot enough to melt substantial portions of the lower mantle (7–9). As debate surrounding core thermal conductivity and implications for Earth's earliest magnetic fields continues (10), there is an ever-increasing need to place robust paleomagnetic constraints on the early geodynamo.

The lack of data before 3.45 Ga leaves a gap of over a billion years in the paleomagnetic record. Attempts to fill this gap have recently focused on the Jack Hills, Western Australia (11), where 2.65–3.05 Ga metaconglomerates contain detrital zircon grains with U–Pb ages as old as 4.4 Ga (12). Although zircon ($ZrSiO_4$) is not itself magnetic, zircon crystals contain inclusions of magnetic minerals that make them potential targets for single-crystal paleomagnetic analysis (13). Tarduno et al. (11) presented a single-crystal paleomagnetic study of Jack Hills detrital zircons, arguing that zircons dated between 3.3 and 4.2 Ga contain primary thermoremanent magnetization (TRM) imparted by an active Hadean to Paleoarchean geodynamo. No microscopy images of primary magnetic carriers within Jack Hills zircon have been presented to date. Rather, there is abundant evidence for secondary magnetic sources on surfaces, along internal cracks, around multiphase microgranite inclusions, and within metamict zones particularly for grains that have not been cleaned with HCl (14). Constraining the source of magnetization—and demonstrating the lack of interference by secondary remanence carriers (15)—is an essential step in confirming the robustness of Hadean paleomagnetism. To this end, we performed a direct study to determine the origin and setting of ferromagnetic carriers in Jack Hills zircon using correlative magnetic measurements and electron microscopy.

Zircon crystals were extracted from metaconglomerates of the Erawandoo Hill Hadean-zircon discovery outcrop (16, 17). We focus primarily on two grains (A and B) that are >3.9 Ga and that passed strict initial selection criteria for potential paleomagnetic targets: lack of evidence for alteration from scanning electron microscopy (SEM) images, concordant U–Pb ages (*SI Appendix*, section E), and treatment with 6M HCl to remove Fe in cracks (14), and a stable natural remanent magnetization (NRM) component (*SI Appendix*, section C). Three broadly defined textures are seen in SEM images: (*i*) primary oscillatory

Significance

The Earth's geodynamo is critical in protecting our atmosphere, and thus plays an important role in the habitability of our planet. As such, the Earth's magnetic field has likely played a crucial role in the emergence of life around 4 billion years ago during the Hadean–Archean Eons. However, we know little about the behavior of the geodynamo during this critical period. Recent efforts have focused on the magnetic signals harbored by Jack Hills zircon crystals, the oldest terrestrial material. Here we show the magnetic carriers in such grains. Our results demonstrate that although ancient zircon grains may contain ideal magnetic recorders, they do not record the magnetic field strength at the time of zircon growth.

Author contributions: R.J.M.T., J.F.E., B.P.W., H.M.W., W.W., P.A.M., T.M.H., and R.J.H. designed research; F.T., R.J.M.T., J.F.E., C.S.B., R.R.F., W.W., L.N., E.A.L., E.A.B., and E.W.A. performed research; W.W. and L.N. contributed new reagents/analytic tools; F.T., R.J.M.T., J.F.E., R.R.F., E.W.A., and R.J.H. analyzed data; and R.J.M.T. and R.J.H. wrote the paper.

The authors declare no conflict of interest.

This article is a PNAS Direct Submission.

Published under the PNAS license.

[1]To whom correspondence should be addressed. Email: rjt79@cam.ac.uk.

This article contains supporting information online at www.pnas.org/lookup/suppl/doi:10.1073/pnas.1811074116/-/DCSupplemental.

Published online December 31, 2018.

zoning, (*ii*) recrystallized zones with bright cathodoluminescence (CL; grain B only), and (*iii*) strongly radiation-damaged metamict zones (individual oscillatory zones in grain A and the entire rim of grain B). Specific areas (Fig. 1) were targeted for scanning transmission electron microscopy (STEM) because of strong magnetic signals observed in the zircon interior using quantum diamond microscopy (QDM) (18). TEM lamellae were extracted from two grains targeting QDM signals within zones displaying primary oscillatory zoning (Fig. 1 *A* and *E*). Sample extraction was after thermal demagnetization experiments for grains A and B, but not for grain C (*SI Appendix*, *SI Appendix*, section A, and *SI Appendix*, Figs. S7–S11). Both heated and nonheated grains displayed identical features. Magnetic regions are observed in areas that display primary zoning and recrystallized zones. Additional images are available in *SI Appendix*, section A.

Grain A ($^{207}Pb^*/^{206}Pb^*$ age = 3979 Ma) clearly displays magnetic signals hosted by primary magmatic zoning in SEM images (Fig. 1 *A*–*D*). However, at the TEM scale, the lamella shows unequivocal microstructural evidence of partial recovery from radiation damage with clearly observed porosity and dislocations (Fig. 2 *A*–*C*). This fluid-absent lattice recovery leads to the formation of nanoscale pores that preferentially nucleate on dislocations, forming strings of pores linked by a common dislocation line that crosscuts primary zonation (Fig. 2*A*). Dislocation cores concentrate nonstructural elements such as Fe and provide fast pipe-diffusion pathways to deliver these elements from external sources to an internal sink (19–21). Direct evidence of this mechanism is seen during the earliest stages of infilling, where Fe accumulates at the intersection of the pore and the dislocation core (Fig. 2*F*). Pores are frequently partially or fully filled with precipitate phases such as magnetite, ilmenite ($FeTiO_3$), and crystalline ZrO_2 (potentially baddeleyite). The result is secondary, dislocation/pore-hosted, nanoscale magnetite grains within zircon that appears unaltered at SEM scale. No magnetite was found that does not lie on secondary microstructures, hence these observations demonstrate that all of the magnetite observed here postdates primary zircon crystallization. A comprehensive set of images of secondary magnetite and associated microstructures in grain A can be found in *SI Appendix*, Fig. S2.

Grain B ($^{207}Pb^*/^{206}Pb^*$ age = 3973 Ma) shows similar features to A in primary oscillatory zoned areas, along with an additional fluid-mediated recrystallization zone also hosting magnetic signals. Recrystallization proceeds as a diffusion–reaction process in which hydrous species diffuse inward and catalyze structural recovery (22, 23). We observe sinuous recrystallization fronts with bright CL, often closely associated with metamict areas that facilitate fluid ingress (Fig. 1*J* and *SI Appendix*, Fig. S5*A*). These recrystallized areas contain defect-rich crystalline zircon and crystallographically oriented precipitates of magnetite with elongated morphology due to preferential growth along intersecting dislocations (*SI Appendix*, Fig. S5*F*). These characteristics are typical of oxide inclusions precipitated from a silicate host by heterogeneous nucleation on dislocations (24, 25) and support a secondary origin for the magnetite in the recrystallized zones. A comprehensive set of images of secondary magnetite and associated microstructures

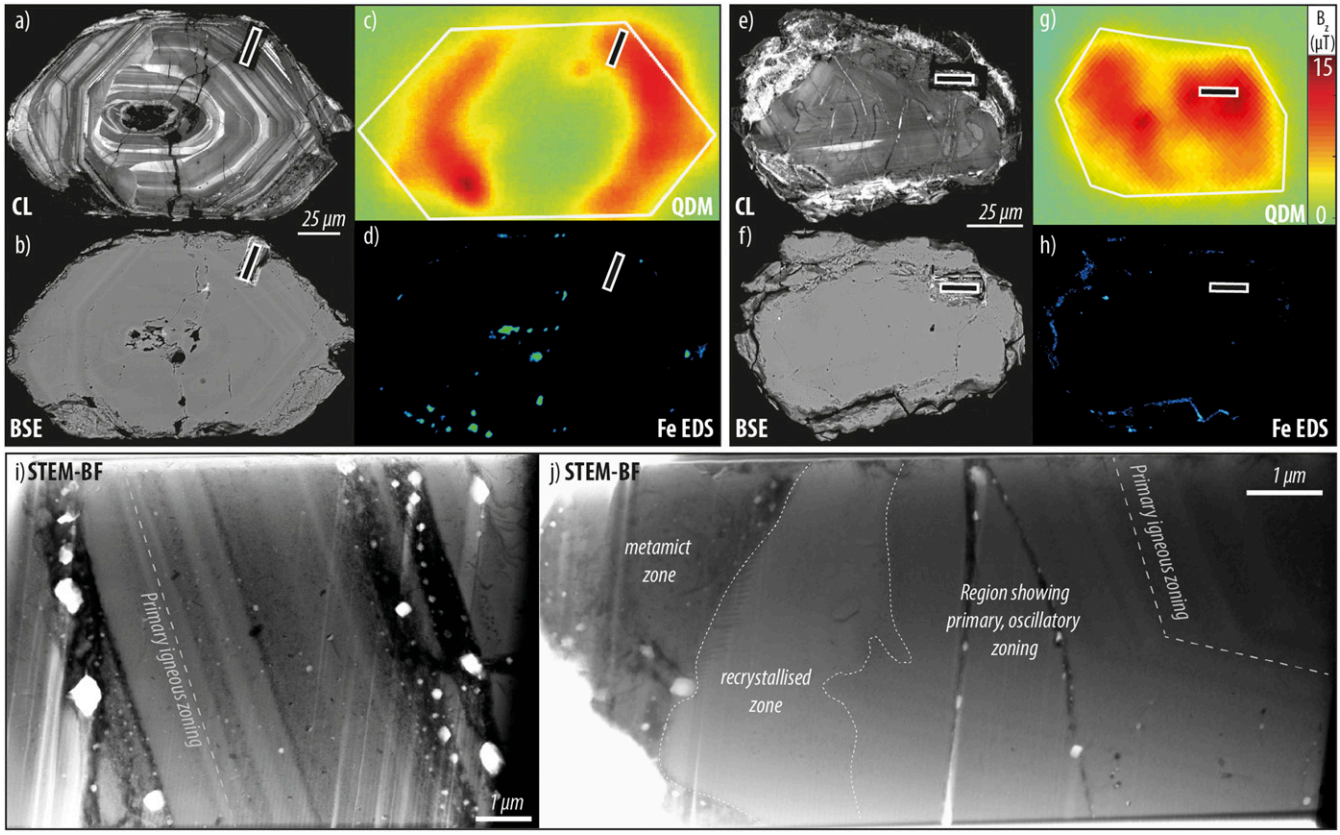

Fig. 1. Summary of SEM (*A*–*H*) and TEM (*I* and *J*) images of Jack Hills zircon grains A and B in this study. White outline rectangles mark original location of TEM lamellae. SEM—grain A: (*A*) CL image showing primary igneous zoning; (*B*) BSE image; (*C*) QDM magnetic anomaly map; and (*D*) compositional map of Fe intensity. Grain B: (*E*) CL image showing primary igneous zoning; (*F*) BSE image; (*G*) QDM magnetic anomaly map; and (*H*) compositional map of Fe intensity. Note that *E* and *F* were taken after a final polish, so that the TEM foil location appears less central than in *G*, which was taken before final polish. (*I*) TEM lamella showing primary zoning and associated secondary inclusions in grain A; and (*J*) TEM lamella showing primary zoning (RHS) and secondary inclusions in grain B. Metamict areas and a fluid-assisted recrystallization zone appear on the LHS. Color scale in *G* also applies to *C*.

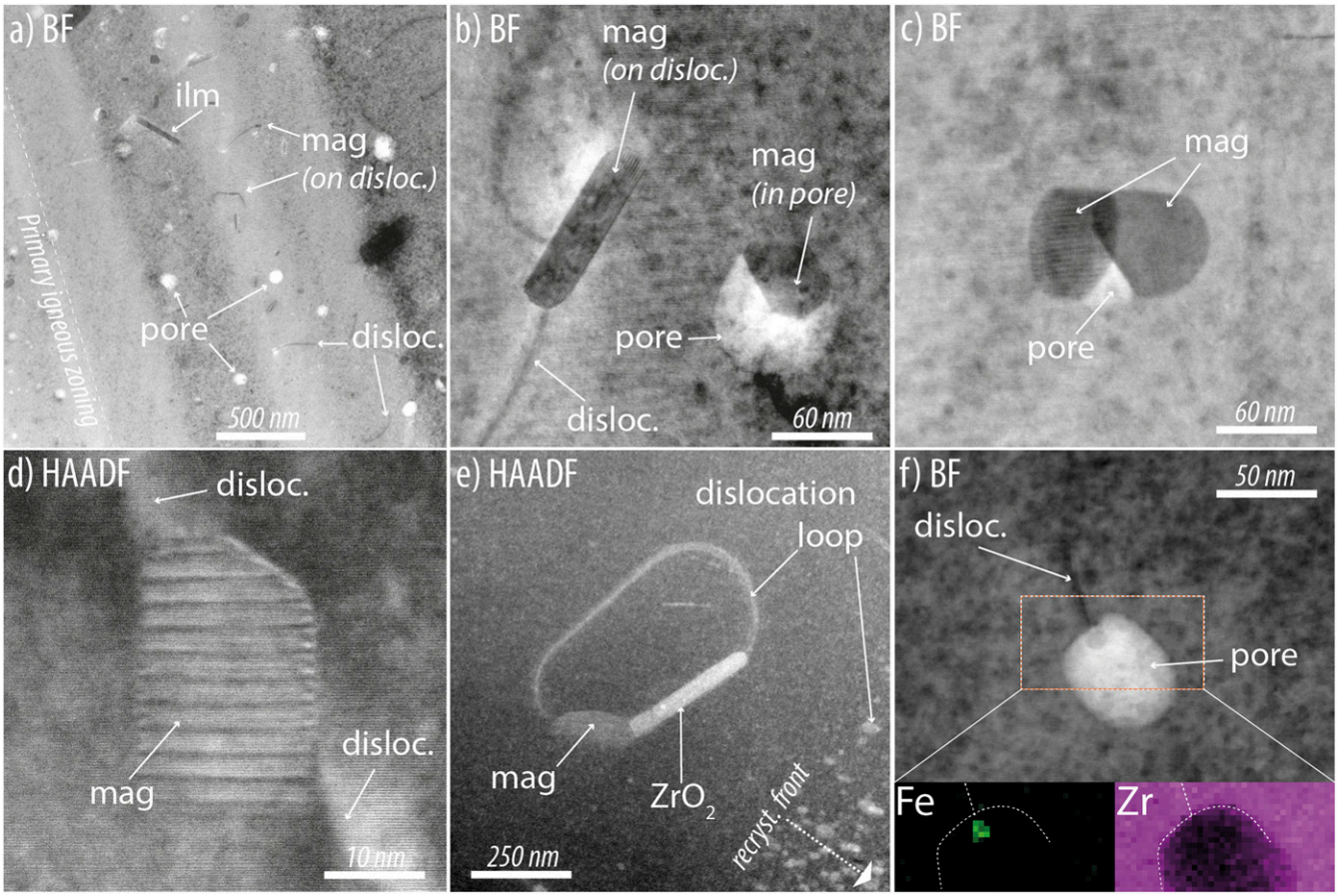

Fig. 2. High-resolution STEM images of nanoscale features and inclusions in this study. Background matrix is zircon. (*A*) Broad view of primary zoning with secondary features related to recovery of radiation damage. (*B*) Secondary magnetite grains along dislocations and filling pore spaces. (*C*) Multiple magnetite crystals in single pore. (*D*) Example of moiré fringe data used to identify magnetite. (*E*) Dislocation loop with magnetite and ZrO_2 near recrystallization front (Fig. 3*E*). (*F*) Intersection of dislocation and pore demonstrating pipe diffusion of secondary Fe into pore spaces; *Insets* show Fe and Zr EDS maps. Mineral abbreviations: ilm, ilmenite; mag, magnetite. Images *A–D* from grain A; image *E* from grain B; images *D* and *F* are from additional grain C (*SI Appendix*, section A). Images *A–C,* grain A; image *E,* grain B; images *D* and *F,* grain C (*SI Appendix*, section A).

in grain B can be found in *SI Appendix*, Figs. S4–S6. Fig. 3 demonstrates the schematic progression of features seen in grain B (Fig. 3*A*). The initial zircon grain shows oscillatory zoning in CL, which reflects a variation in trace element content, e.g., U, and a high-U rim (Fig. 3*B*). Radiation damage slowly accumulates in the core, and the high-U rim becomes totally metamict. Partial annealing of the core results in linked pore-dislocation networks, and the high-U rim facilitates fluid ingress at a later stage, reorganizing the annealing microstructures (Fig. 3 *C* and *F* and *SI Appendix*, Fig. S5*A*). Magnetite growth in the core can only take place once this network of secondary features has accumulated (Fig. 3 *D*, *F*, and *G* and *SI Appendix*, Fig. S4 *A–D*), and must therefore significantly postdate zircon crystallization.

Clear identification of the Fe-oxide as magnetite is the result of correlating the various datasets. Fe-oxides observed chemically from STEM energy dispersive spectroscopy (EDS) were observed using moiré fringe lattice interference patterns between the zircon and oxide. The resultant moiré fringe d-spacing (Fig. 2*D* and *SI Appendix*, Fig. S11) defines the Fe-oxide as most likely magnetite, with a possibility of being maghemite. However, the paleomagnetic data showing complete NRM demagnetization by 580 °C means it is only possible for the inclusions to be magnetite (*SI Appendix*, Fig. S13). The extraction of robust Hadean paleomagnetic signals from zircon single crystals relies on the following assumptions about any given magnetic particle: (*i*) iron oxide grains became trapped as primary inclusions in igneous zircon; (*ii*) inclusions within the zircon acquired a primary TRM during postcrystallization cooling and have not been subsequently reheated above the Curie temperature; (*iii*) armoured magnetic inclusions remained chemically and thermally unaltered by pre- and postdepositional high-temperature metamorphic and low-temperature aqueous alteration/recrystallization events; and (*iv*) the high-temperature component of primary TRM can be separated from overlapping sources of secondary magnetization. If all these conditions are met, then the Jack Hills zircons have the potential to constrain the properties of the Hadean geodynamo. If any one of these conditions is violated, the case for primary magnetization cannot be made.

We have observed two pathways for the formation of secondary single-domain magnetite in Jack Hills zircon, circumventing criteria (*i*) and (*iii*) above. Formation of secondary magnetite in the presence of a magnetic field will generate a chemical remanent magnetization (CRM). An important property of CRM is that its thermal unblocking temperature is not limited by the temperature of its acquisition, but by the volume of the particles formed (26). Magnetite particles of sufficient size acquire CRM with laboratory unblocking temperatures that overlap with the 550–585 °C window attributed to primary Hadean remanence (27). A representative (but not exhaustive) summary of magnetite particles observed using TEM is given in *SI Appendix*, Table S1. Measurements of the length (L) and width (W) of each particle were taken directly from the TEM images. Fig. 4 compares the 2D projected lengths and

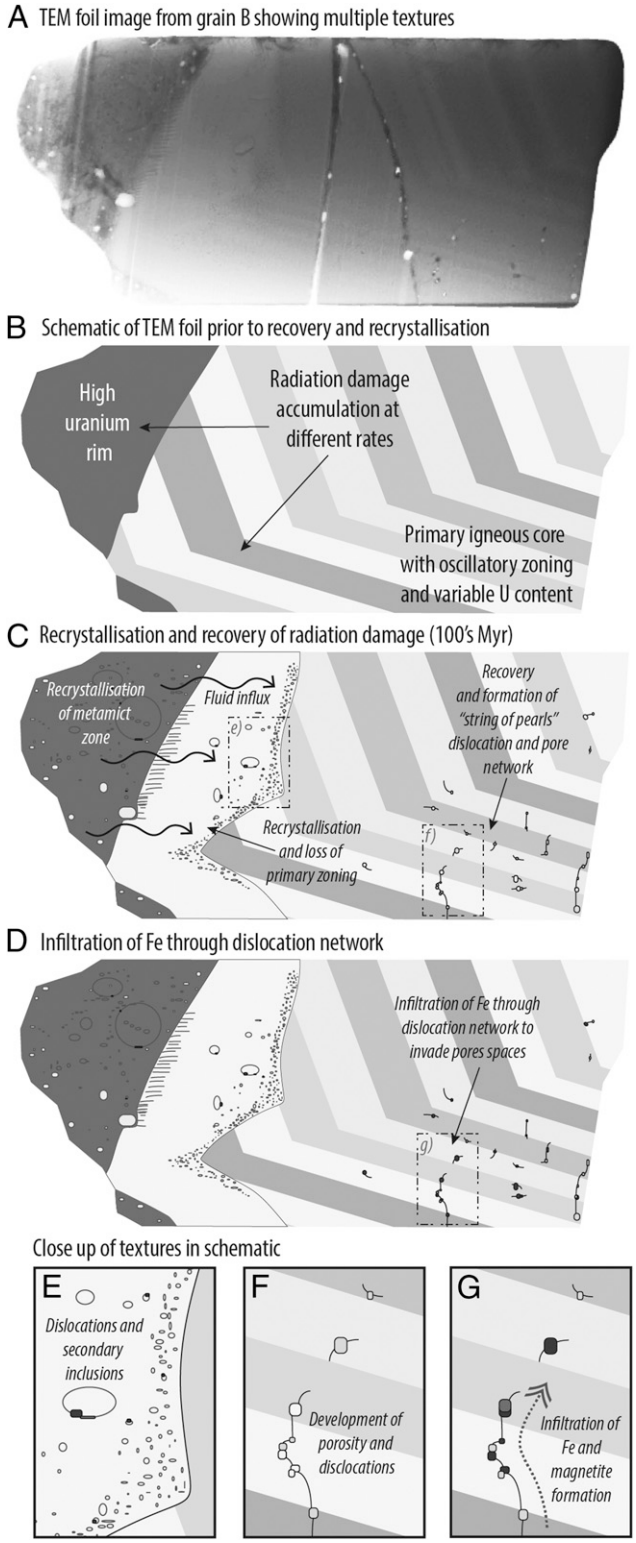

Fig. 3. Summary diagram showing order of events forming secondary inclusions in grain B. (*A*) TEM BF image of lamella. (*B*) Schematic of zoning in zircon. Oscillatory zoning with variable U content (light = low U) accumulating radiation damage at different rates. High-U rim area accumulates damage most rapidly. (*C*) Fluid-mediated recrystallization and fluid-absent recovery process occur 100s My after grain formation. (*D*) Fe infiltrates dislocation-pore network forming magnetite. (*E–G*) Close up of processes *Inset* areas in *C* and *D*. Features shown in *F* and *G* are clear in images from *SI Appendix*, Fig. S4 *A–D*.

aspects ratios of the observed particles with the calculated thresholds for superparamagnetic, single-domain, and vortex behavior in isolated magnetite particles (28). The majority of observed particles are predicted to be single domain (Fig. 4*A*), with 40% of grains having blocking temperatures >500 °C (Fig. 4*B*). Two of the largest particles observed are predicted to lie above the threshold for single-vortex behavior for noninteracting magnetite (28). Micromagnetic simulations confirm that these particles adopt either single-domain or single-vortex states at remanence, that both adopt vortex states during magnetization reversal, and that their blocking temperatures are 570–575 °C (*SI Appendix*, section D). Single-vortex particles of a similar size have been observed to retain their remanence all of the way to the Curie temperature (29). Thermal demagnetization of grain A demonstrates that 30–40% of its NRM is retained after heating to 550 °C in zero field and that the NRM is fully demagnetized by 580 °C (*SI Appendix*, section C), confirming the presence of magnetite remanence carriers with high blocking temperatures. This means that a putative primary Hadean TRM and secondary CRM would have overlapping blocking spectra, making it difficult to discriminate primary and secondary remanence, violating criteria (*iv*) above.

Given these observations of secondary ferromagnetism, recognizing the presence of (or demonstrating the lack of) secondary magnetite via high-resolution magnetic, compositional, and mineralogical analyses are now essential steps in the quest for Hadean paleomagnetism. Although most magnetite particles formed through fluid-mediated recrystallization that we observed fall well within the stable single-domain size range, their frequently low volumes yield blocking temperatures that mostly lie outside the 550–585 °C window used to isolate Hadean remanence. Therefore, CRM acquired via this mechanism might be avoided through careful sample characterization and thermal demagnetization to 550 °C (27). However, the formation of secondary magnetite in crystalline zircon via the pipe-diffusion mechanism cannot be recognized using CL imaging, is not associated with Pb loss, and produces magnetite particles with sizes and aspect ratios spanning the stable single-domain to single-vortex range, with blocking temperatures that fall within the 550–585 °C window.

Evaluation of the TEM images in this study enables an estimate to be made of the volume expansion of the crystal lattice due to radiation damage. Image analysis of the ratio of zircon to observed pore spaces shows a volume expansion of ∼0.7%, used as a proxy for lattice expansion, which can be converted to the time taken to accumulate this damage based on the original actinide content (30). Back-calculated U and Th concentrations give a lower estimate of c. 950 and c. 500 My for grains A and B, respectively, to produce the observed porosity (*SI Appendix*, section B provides more details). This means that the Fe source may be from fluid alteration within precursor igneous rocks, but also allows for the source of Fe to be the Jack Hills sediment itself, consistent with deep weathering estimates (31). This estimate provides an upper age limit for magnetite formation, and is clearly significantly later than zircon crystallization (Fig. 3).

The distinct possibility that the secondary Fe source predates sedimentation at 3.0 Ga is important, as it negates the use of microconglomerate tests on the Jack Hills sediments as evidence for primary magnetization. The observed radiation damage in Jack Hills zircon is much lower than that expected on the basis of their actinide content and age (32). Therefore, this pipe-diffusion mechanism is expected to be widespread, a natural consequence of the build up and subsequent recovery of radiation damage that will affect all ancient zircon crystals. Therefore, unless primary magnetite can be confirmed, the existence of a magnetic field during Eoarchean and Hadean remains an unknown.

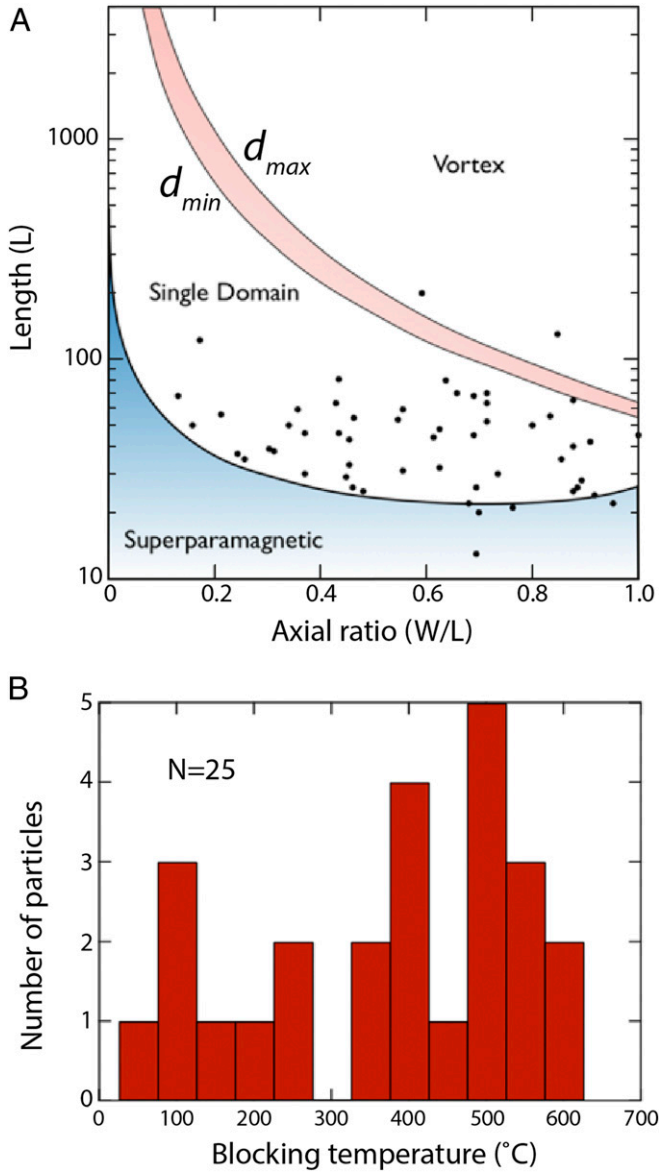

Fig. 4. Magnetic information on secondary magnetite particles observed in Jack Hills zircon. (*A*) *L* vs. aspect ratio (*W*/*L*) for magnetite particles observed using TEM (*SI Appendix*, Table S1). Boundaries between superparamagnetic, single-domain, and vortex states are based on micromagnetic simulations of noninteracting magnetite (28). (*B*) Histogram of calculated blocking temperatures (50 °C bin width), excluding SP particles. Blocking temperatures were calculated for laboratory observation times (taken to be t_{obs} = 100 s). A significant number of the particles observed have T_B > 500 °C, consistent with the rapid loss of NRM observed using superconducting quantum interference device (SQUID) magnetometry (*SI Appendix*, Fig. S13).

Methods

SEM. An FEI Quanta 650 field emission gun SEM was used to collect both energy dispersive spectroscopy elemental maps (at 20 kV accelerating voltage), backscattered electron (BSE), and cathodoluminescence micrographs (collected at 5 kV). The BSE and CL maps were collected in parallel, and the EDS maps were collected subsequently. EDS maps were collected using two Bruker 6|30 EDS detectors simultaneously to increase the overall counts and improve throughput. For grain C, each pixel's spectrum was denoised using a Python-based nonnegative matrix factorization algorithm, background subtracted, and then peak integration performed on the $Fe_{K\alpha}$ window of 6.0–6.7 keV (33, 34).

TEM. The TEM specimen was site-precisely prepared from a zircon grain using a dual beam focused ion beam (FIB) scanning electron microscope field electron and ion (FEI), now Thermo Fisher Scientific, Helios NanoLab. An in situ lift-out technique was applied to extract and transfer the specimen onto a standard TEM molybdenum half grid, and a platinum bar was deposited on the surfaces of target areas before FIB processing. The TEM lamella was made with the reduced FIB voltages down to ∼2–5 kV to minimize FIB-induced damage (35), and was cleaned for about 3–5 min in a plasma chamber before being loaded into the TEM microscope. The TEM study was carried out using two microscopes: FEI Tecnai Osiris and FEI Titan^3 (80–300 kV), and both were dedicated to scanning TEM operation. The Osiris microscope fitted with four silicon drift detectors for energy dispersive X-ray spectrometry analysis was used for STEM high-angle annular dark field (HAADF) and STEM-bright field (BF) imaging and fast STEM chemical mapping operating at 200 kV. The Titan microscope had a probe-forming corrector for spherical aberration, allowing for high resolution imaging in STEM configuration at 300 kV. To obtain optimum contrast for identifying nanometer-sized particles, the STEM imaging was typically taken at the combination of the camera length between 80 and 250 mm and the screen currents of 0.05–0.3 nA; whereas, the STEM chemical mapping was performed at the screen currents larger than about 0.1 nA.

U–Pb Geochronology. Grains were prescreened for ancient Pb isotope signatures on the CAMECA ims1270 ion microprobe using a 15-nA O-primary beam and a mass resolution of 5000. This used more rapid count times to analyze a large number of grains but at lower than normal precision. Oxygen flooding to c. 1 × 10-5 torr was used to enhance Pb ionization. Following a 2-min presputter to clean the zircon surface, Pb isotopes were counted for 30 s in monocollection mode. During a later session, U–Pb ages were measured under the more typical instrumental conditions and count times, using the AS3 zircon standard (36) for Pb/U relative sensitivity factor calibration. More details on the U–Pb method can be found in Quidelleur et al. (37).

QDM. We use the quantum diamond microscope at the Harvard Paleomagnetics Laboratory to obtain high-resolution magnetic field maps of zircon grains A and B (Fig. 1 *C* and *G*). Both grains are first subjected to a 0.25 T isothermal remanent magnetization oriented out of the imaging plane. The polished surface of the zircons is then placed in contact with the sensing diamond, which has nitrogen-vacancy (*N*-V) centers implanted uniformly in a 4-μm layer. We then optically excite the (*N*-V) centers with a 500-mW 532-nm wavelength laser and image the fluorescence at a spatial resolution of 1.17 μm per pixel. To maximize the signal-to-noise ratios, we perform the experiments in projective magnetic microscopy mode (18) that directly measures the magnetic field projection in the [111] direction of the diamond lattice. This protocol involves two measurements taken under bias fields of 900 μT oriented in opposing directions parallel to the [111] axis. The two maps are then summed to isolate the ferromagnetic component. The reversal accuracy of the bias field is 1 part in 1500, resulting in a residual bias field of 600 nT, which is then subtracted from the summed map. The residual bias field in the final map is therefore at least 10^3 smaller than the zircon signals and can be neglected. We then convert these projected magnetic field values to the magnetic field perpendicular to the measurement plane using spectral domain algorithm (38).

Laser Ablation. U and Th measurements were made for the zircon grains alongside the TEM locations to calculate radiation damage times. Analyses were carried out using an ESI UP193UC laser system coupled to a Perkin–Elmer Nexion 350D inductively coupled plasma mass spectrometer (LA-ICP-MS) in the Department of Earth Sciences at the University of Cambridge. The LA-ICP-MS data acquisition settings were 1 sweep per reading, 80 readings, 1 replicate, and total data acquisition lasted 50 s (∼1 data point for each element per second). The instrument was set up for background data followed by ablation for 20 s, at a rep rate of 10 Hz, and power on the sample of ∼3 joules per cm^2. Data were processed using Iolite software with the trace element DRS (39), with concentrations calibrated against KLDF standard zircon (Curtin University internal standard; U 507 ppm, Th 75 ppm) and 91500 (40). National Institute of Standards and Technology glasses SRM 610 and 612 (41) were run to monitor instrument stability. U and Th concentrations were calculated for the crystallization ages of the grains.

ACKNOWLEDGMENTS. We thank two anonymous reviewers for their constructive comments that greatly improved the manuscript. The research leading to these results has received funding from the European Research Council under the European Union's Seventh Framework Programme (Grant FP/2007-2013)/European Research Council Grant Agreement 320750, Natural Environment Research Council Grant NE/P002498/1, National Science Foundation (NSF) Grant EAR1647504, and Thomas F. Peterson, Jr. The University of California, Los Angeles ion microprobe facility is partly supported by a grant from the Instrumentation and Facilities Program, Division of Earth Sciences, NSF (1339051).

1. Tarduno JA, et al. (2010) Geodynamo, solar wind, and magnetopause 3.4 to 3.45 billion years ago. *Science* 327:1238–1240.
2. Biggin AJ, et al. (2011) Palaeomagnetism of Archaean rocks of the Onverwacht Group, Barberton greenstone belt (southern Africa): Evidence for a stable and potentially reversing geomagnetic field at ca. 3.5Ga. *Earth Planet Sci Lett* 302:314–328.
3. McElhinny M, Senanayake W (1980) Paleomagnetic evidence for the existence of the geomagnetic field 3.5 Ga ago. *J Geophys Res Solid Earth* 85:3523–3528.
4. Gomi H, et al. (2013) The high conductivity of iron and thermal evolution of the Earth's core. *Phys Earth Planet Inter* 224:88–103.
5. Pozzo M, Davies C, Gubbins D, Alfè D (2013) Transport properties for liquid silicon-oxygen-iron mixtures at Earth's core conditions. *Phys Rev B* 87:014110.
6. Ohta K, Kuwayama Y, Hirose K, Shimizu K, Ohishi Y (2016) Experimental determination of the electrical resistivity of iron at Earth's core conditions. *Nature* 534: 95–98.
7. Davies C, Pozzo M, Gubbins D, Alfè D (2015) Constraints from material properties on the dynamics and evolution of Earth's core. *Nat Geosci* 8:678–685.
8. O'Rourke JG, Korenaga J, Stevenson DJ (2017) Thermal evolution of Earth with magnesium precipitation in the core. *Earth Planet Sci Lett* 458:263–272.
9. Badro J, Siebert J, Nimmo F (2016) An early geodynamo driven by exsolution of mantle components from Earth's core. *Nature* 536:326–328.
10. Konôpková Z, McWilliams RS, Gómez-Pérez N, Goncharov AF (2016) Direct measurement of thermal conductivity in solid iron at planetary core conditions. *Nature* 534:99–101.
11. Tarduno JA, Cottrell RD, Davis WJ, Nimmo F, Bono RKA (2015) PALEOMAGNETISM. A Hadean to Paleoarchean geodynamo recorded by single zircon crystals. *Science* 349: 521–524.
12. Valley JW, et al. (2014) Hadean age for a post-magma-ocean zircon confirmed by atom-probe tomography. *Nat Geosci* 7:219–223.
13. Fu RR, et al. (2017) Evaluating the paleomagnetic potential of single zircon crystals using the Bishop Tuff. *Earth Planet Sci Lett* 458:1–13.
14. Weiss BP, et al. (2018) Secondary magnetic inclusions in detrital zircons from the Jack Hills, Western Australia, and implications for the origin of the geodynamo. *Geology* 5: 427–430.
15. Weiss BP, et al. (2015) Pervasive remagnetization of detrital zircon host rocks in the Jack Hills, Western Australia and implications for records of the early geodynamo. *Earth Planet Sci Lett* 430:115–128.
16. Maas R, Kinny PD, Williams IS, Froude DO, Compston W (1992) The Earth's oldest known crust: A geochronological and geochemical study of 3900-4200 Ma old detrital zircons from Mt. Narryer and Jack Hills, Western Australia. *Geochim Cosmochim Acta* 56:1281–1300.
17. Wilde SA, Valley JW, Peck WH, Graham CM (2001) Evidence from detrital zircons for the existence of continental crust and oceans on the Earth 4.4 Gyr ago. *Nature* 409: 175–178.
18. Glenn DR, et al. (2017) Micrometer-scale magnetic imaging of geological samples using a quantum diamond microscope. *Geochem Geophys Geosyst* 18:3254–3267.
19. Piazolo S, et al. (2016) Deformation-induced trace element redistribution in zircon revealed using atom probe tomography. *Nat Commun* 7:10490.
20. Timms NE, Reddy SM, Gerald JDF, Green L, Muhling JR (2012) Inclusion-localised crystal-plasticity, dynamic porosity, and fast-diffusion pathway generation in zircon. *J Struct Geol* 35:78–89.
21. White LF, et al. (2017) Atomic-scale age resolution of planetary events. *Nat Commun* 8:15597.
22. Geisler T, Schaltegger U, Tomaschek F (2007) Re-equilibration of zircon in aqueous fluids and melts. *Elements* 3:43–50.
23. Geisler T, Pidgeon RT, Kurtz R, van Bronswijk W, Schleicher H (2003) Experimental hydrothermal alteration of partially metamict zircon. *Am Mineral* 88:1496–1513.
24. Lappe S-CLL, et al. (2011) Mineral magnetism of dusty olivine: A credible recorder of pre-accretionary remanence. *Geochem Geophys Geosyst* 12:Q12Z35.
25. Einsle JF, et al. (2016) Multi-scale three-dimensional characterization of iron particles in dusty olivine: Implications for paleomagnetism of chondritic meteorites. *Am Mineral* 101:2070–2084.
26. McClelland-Brown E (1982) Discrimination of TRM and CRM by blocking-temperature spectrum analysis. *Phys Earth Planet Inter* 30:405–414.
27. Tarduno JA, Cottrell RD (2013) Signals from the ancient geodynamo: A paleomagnetic field test on the Jack Hills metaconglomerate. *Earth Planet Sci Lett* 367:123–132.
28. Muxworthy AR, Williams W (2009) Critical superparamagnetic/single-domain grain sizes in interacting magnetite particles: Implications for magnetosome crystals. *J R Soc Interface* 6:1207–1212.
29. Almeida TP, et al. (2016) Direct visualization of the thermomagnetic behavior of pseudo-single-domain magnetite particles. *Sci Adv* 2:e1501801.
30. Murakami T, Chakoumakos BC, Ewing RC, Lumpkin GR, Weber WJ (1991) Alpha-decay event damage in zircon. *Am Mineral* 76:1510–1532.
31. Pidgeon RT, Nemchin AA, Whitehouse MJ (2017) The effect of weathering on U–Th–Pb and oxygen isotope systems of ancient zircons from the Jack Hills, Western Australia. *Geochim Cosmochim Acta* 197:142–166.
32. Pidgeon R (2014) Zircon radiation damage ages. *Chem Geol* 367:13–22.
33. Lee DD, Seung HS (1999) Learning the parts of objects by non-negative matrix factorization. *Nature* 401:788–791.
34. de la Peña F, et al. (2017) Data from "hyperspy/hyperspy: HyperSpy 1.1.2." Zenodo. Available at https://zenodo.org/record/240660.
35. Tang F, et al. (2018) Nanoscale structural and chemical analysis of F-implanted enhancement-mode InAlN/GaN heterostructure field effect transistors. *J Appl Phys* 123:024902.
36. Paces JB, Miller JD (1993) Precise U-Pb ages of Duluth complex and related mafic intrusions, northeastern Minnesota: Geochronological insights to physical, petrogenetic, paleomagnetic, and tectonomagmatic processes associated with the 1.1 Ga midcontinent rift system. *J Geophys Res Solid Earth* 98:13997–14013.
37. Quidelleur X, et al. (1997) Thermal evolution and slip history of the Renbu Zedong Thrust, southeastern Tibet. *J Geophys Res Solid Earth* 102:2659–2679.
38. Lima EA, Weiss BP (2009) Obtaining vector magnetic field maps from single-component measurements of geological samples. *J Geophys Res Solid Earth* 114: B06102.
39. Paton C, Hellstrom J, Paul B, Woodhead J, Hergt J (2011) Iolite: Freeware for the visualisation and processing of mass spectrometric data. *J Anal At Spectrom* 26: 2508–2518.
40. Wiedenbeck M, et al. (2004) Further characterisation of the 91500 zircon crystal. *Geostand Geoanal Res* 28:9–39.
41. Pearce NJG, et al. (1997) A compilation of new and published major and trace element data for NIST SRM 610 and NIST SRM 612 glass reference materials. *Geostand Newsl* 21:115–144.

Secondary magnetite in ancient zircon precludes analysis of a Hadean geodynamo

Fengzai Tang[a], Richard J. M. Taylor[a1], Josh F. Einsle[a,b], Cauê S. Borlina[c], Roger R. Fu[d], Benjamin P. Weiss[c], Helen M. Williams[a], Wyn Williams[e], Lesleis Nagy[f], Paul A. Midgley[b], Eduardo A. Lima[c], Elizabeth A. Bell[g], T. Mark Harrison[g], Ellen W. Alexander[g], Richard J. Harrison[a]

1. corresponding author email: rjt79@cam.ac.uk

This PDF file includes:

Supplementary Appendix Sections A-E
- A) Additional TEM images
  - Grain A : S1 – S2
  - Grain B : S3 – S6
  - Grain C : S7 – S11
- B) Radiation damage model: S12
- C) Paleomagnetic data: S13
- D) Micromagnetic modelling: S14
- E) Uranium-Lead dating: S15

Figs. S1 to S15
Legends for Supplementary Movies S1 to S2
References for SI reference citations
Table S1

Other supplementary materials for this manuscript include the following:

Movies S1 to S2

Supplementary information A – Additional grain information and images

Original grain names in research project:

Grain A – 080211_h30

Grain B – 071320_h02

Grain C – D175M-B2-1-4

Grain A

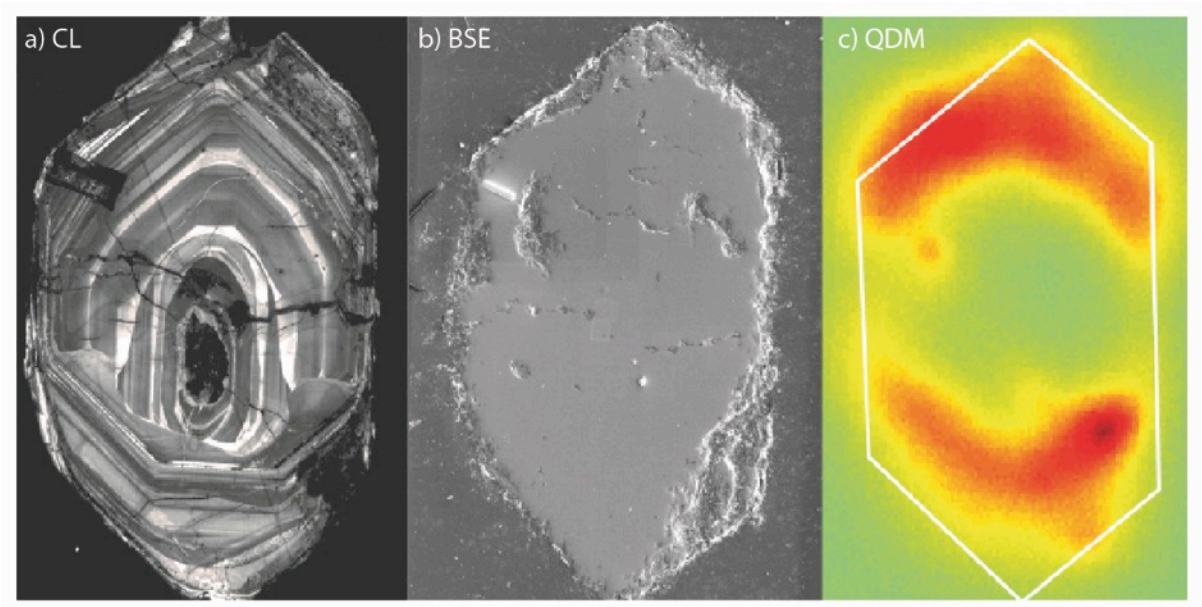

Supplementary Figure S1. SEM and magnetic images of Grain A. This zircon at first glance may appear to be a good example of a potential paleomagnetic target for the early Earth. It shows almost uniform, continuous oscillatory zoning indicative of primary igneous growth. The CL image does not show any significant recrystallization zones, or metamorphic overgrowths. Other than a few late cracks, the BSE image is very flat, suggesting a good grain quality. The QDM image highlights magnetic portions of the grain that are spatially associated with the primary zoning, suggesting the incorporation of primary magnetite during crystallisation. However, a TEM foil extracted from one such zone (top left in images) found that all magnetite is associated with secondary recrystallization features.

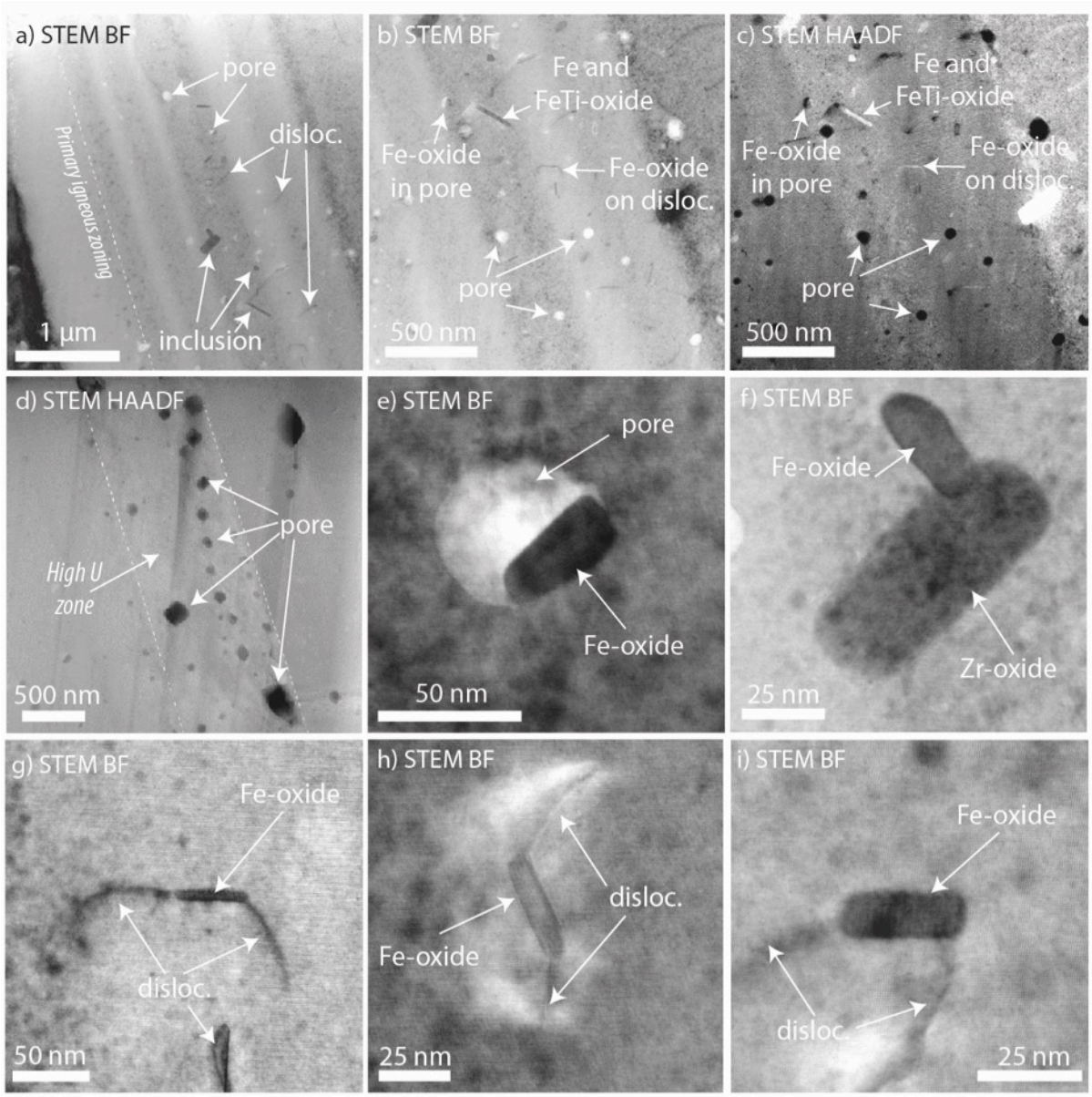

Supplementary Figure S2. STEM images of TEM foil extracted from Grain A. a) Overview BF image, highlighting the contrast between primary oscillatory zones, secondary microstructures, pores and inclusions. b-c) BF and HAADF image of the same area, demonstrating the contrast of various features used to identify microstructures and inclusions. Images are dominated by the zircon matrix in mid grey, showing primary zoning. The BF image shows low density features such as pore spaces as bright areas, whilst high-density inclusions such as magnetite, ZrO_2 and ilmenite appear slightly darker. HAADF image shows opposing greyscale with density, and highlights some features more clearly. d) Image showing one of the more radiation-damaged (higher U) primary zones (see main text Figure 1i). Initially these areas were investigated as potential sources of magnetism, but they were found to be dominated by empty pore space and very few inclusions compared to other zones. e) Example of Fe-oxide grain partially filling a pore space that was generated through recovery of radiation damage. f) Example of Fe-oxide grain associated with other secondary inclusions, in this

case ZrO_2. g-i) Multiple examples of typical magnetic sources observed in recovered, oscillatory zoned area. Fe-oxide particles are elongate and associated with secondary dislocation microstructures.

Grain B

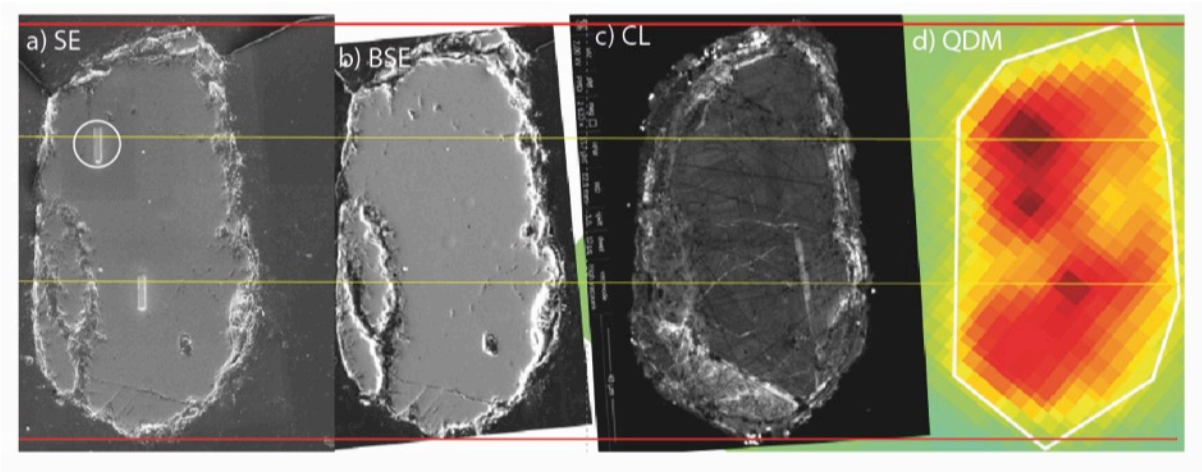

Supplementary Figure S3. SEM and magnetic images of Grain B used for targeting prior to extraction of TEM foil. Left to right: SE, BSE, CL, QDM. QDM images shows locations of target areas of interest prior to the TEM study. White circle shows location of TEM extraction site (second site near centre of grain was not studied). This supplementary figure set shows the true location of the TEM foil with respect to targeting images, and can be seen to be predominantly within the core (oscillatory zoned region) of the grain. However, the polish at this stage was not suitable for CL imaging. The main manuscript figures give the impression the foil was extracted more in the metamict rim; however, this was after an additional polish to show the internal features in CL.

Grain B is made up of 3 distinct zones: an oscillatory zoned core, representing igneous crystallisation and recovered radiation damage; a highly radiation-damaged zone around the edge of the grain; and a zone in between which shows evidence of fluid assisted recrystallization. Zones showing primary zoning and recrystallization textures show nanoscale magnetite particles responsible for secondary magnetic signals. The TEM foil for this grain traverses all three zones showing multiple examples of Fe-oxide inclusions. Late cracks are seen through the core, which may accommodate a number of macroscale secondary features, and are not the focus of this study (see Weiss et al., 2018). Additional images to compliment the main text are shown below.

Oscillatory zoned core "recovery zone"

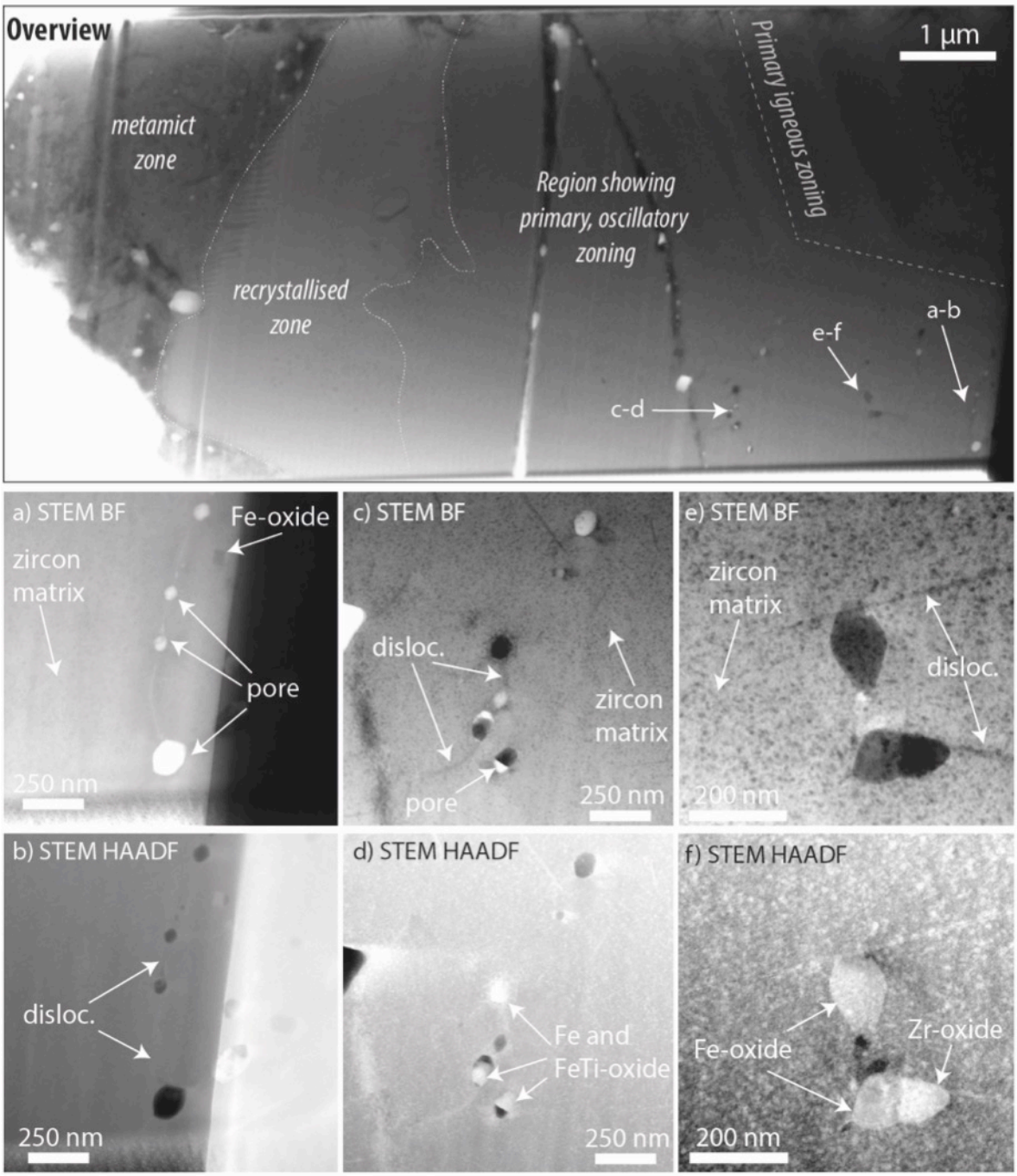

Supplementary Figure S4. STEM images of TEM foil extracted from Grain B core. Overview is from main text figure 1j and shows the majority of the sample, centre and RHS as oscillatory zoned with two crystal faces present. Each pair show a BF and HAADF image of a target area to highlight typical features and sizes. All inclusions are on secondary features but are clearly shown to be within primary oscillatory zoning. a-b) Images show the common "string of pearls" configuration seen in zones that have recovered from minor radiation damage (main text Figure 3). Pore spaces, accommodating the volume expansion, are joined by dislocation features. This setup provides a favorable scenario for pipe diffusion of Fe into sink regions (main text Figure 2f). c-d) Images

showing the partially filled pores with a variety of typical inclusion chemistries. Infilling of Fe and Ti is facilitated by dislocations acting as diffusion pathways into the oscillatory zoned interior of the grain. e-f) Examples of some of the largest magnetite grains associated with dislocations observed in this study. TEM tilt analysis gives maximum dimensions of 200 × 110 nm for the upper, octahedral grain (Fe_#21 in Supplementary Table 1; see Supplementary Information D for micromagnetic simulations of this particle).

Fluid-assisted recrystallization zone

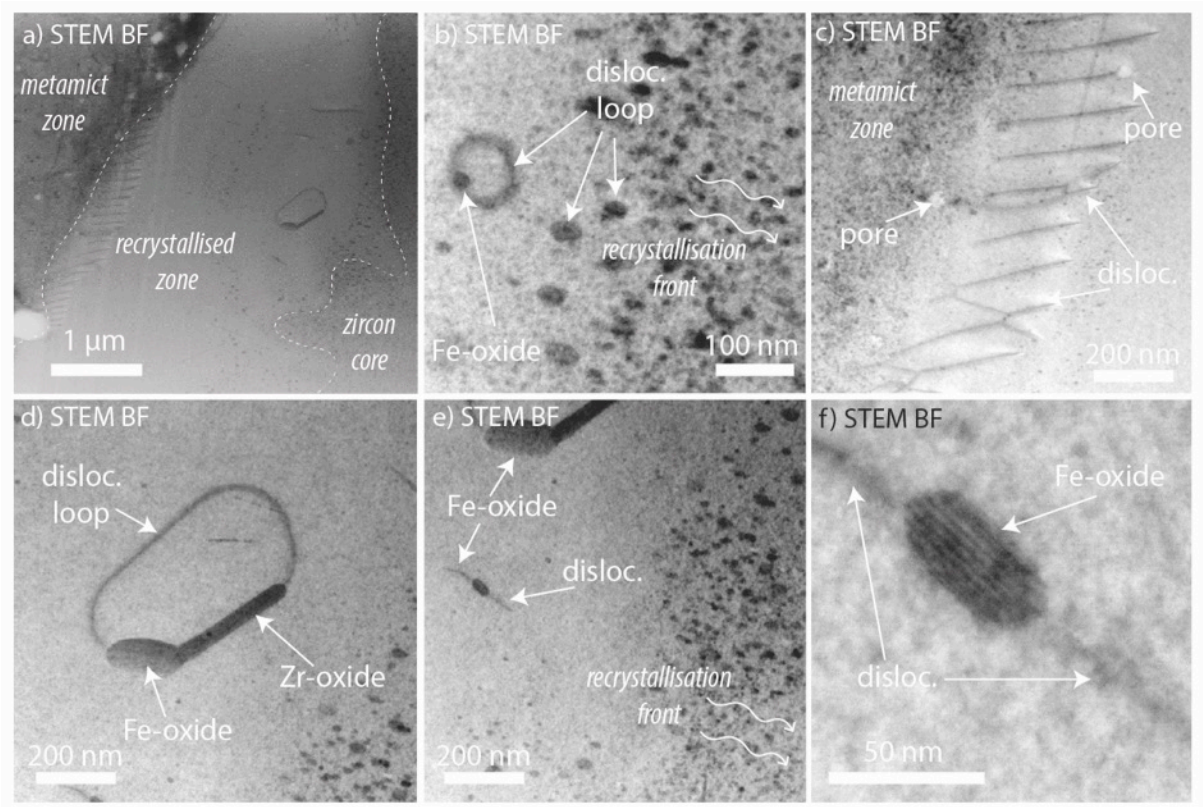

Supplementary Figure S5. STEM-BF images of TEM foil extracted from Grain B recrystallised zone. a) Overview of the recrystallised zone. Zircon matrix has undergone a fluid assisted diffusion-reaction process that has removed primary zoning but left behind a magnetite-bearing microstructure. Recrystallised zone is bounded to the right by the oscillatory zoned core, and to the left by the high U metamict zone, that may serve as a fluid ingress pathway. b) Boundary between the recrystallised zone and zircon core. This sinuous region is dominated by nanoscale dislocation loops resulting from the recrystallization process. Loops appear to increase in size away from the front and may be decorated with Fe-oxides in a "diamond ring" structure. c) Boundary between recrystallised zone and metamict area. This area displays stacked dislocation features and some associated porosity. d) The core of the recrystallised zone typically displays fewer, larger features than the boundaries. This large dislocation loop is the site of an Fe-oxide >150 nm in length and an elongate baddeleyite crystal (Fe_#32 in Supplementary Table 1; see Supplementary Information D for micromagnetic simulations

of this particle). e-f) Two magnifications of secondary Fe-oxide grains displaying the typical elongate nature, having grown with long axis parallel to associated dislocation features.

High U metamict zone

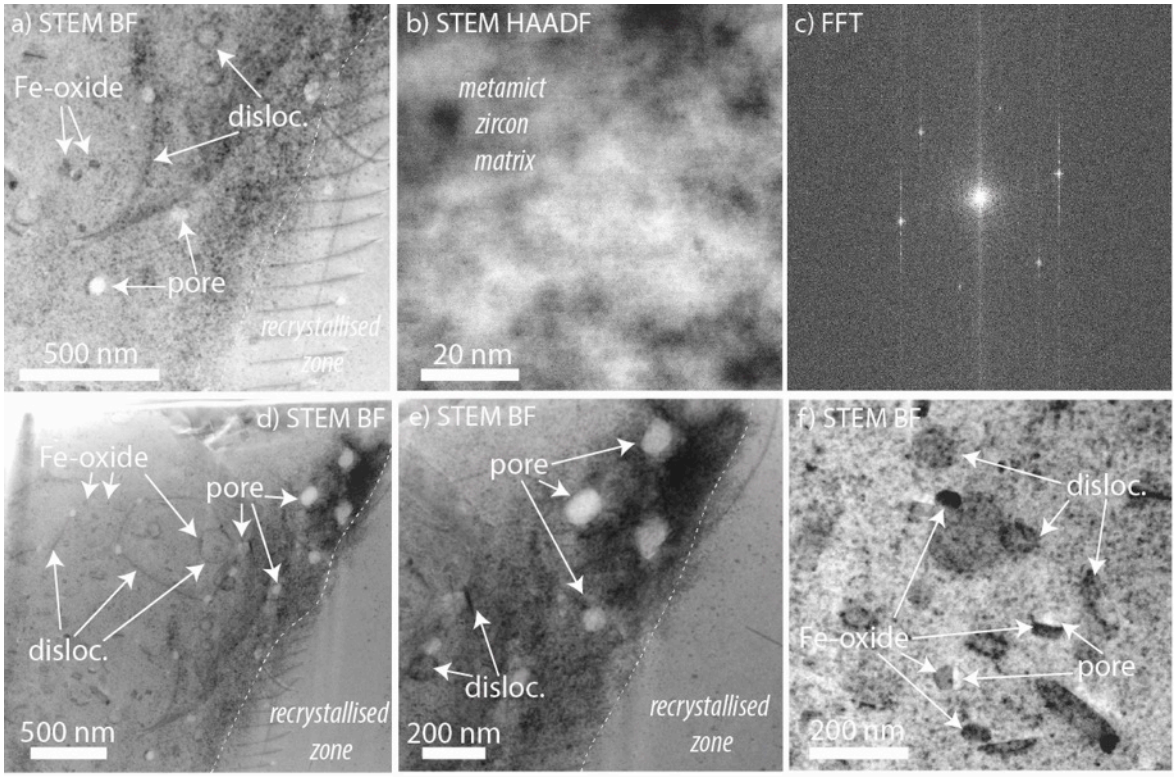

Supplementary Figure S6. STEM images of TEM foil extracted from Grain B metamict zone zone. a) Overview of the metamict zone. The zircon matrix in this area shows a more mottled appearance, indicative of higher degrees of radiation damage than has occurred in other parts of the grain, including loss of primary zoning. Whilst characterisation of this area was not a priority – due to highly damaged grains not being good paleomagnetic targets – the features present are still of general interest in relation to the recrystallization processes at work. Evidence of recovery of radiation damage is present in the form of pore space and dislocations, though of a higher density than seen in the grain core. Fe-oxide particles are associated with these features as seen in other areas. b) Close up image of the mottled texture of the zircon matrix. c) Fast fourier transform (FFT) of previous image demonstrates that the matrix is at least semi crystalline. This suggests that metamictisation has left islands of more pristine zircon, or that the matrix has recrystallised during fluid assisted processes. The latter is supported by the microstructures seen. d-f) Images at a variety of scales showing the density and relationship of microstructures and associated Fe-oxide particles. Additional work on grain C suggests metamict zone Fe-oxides may be dominated by hematite.

Grain C

Grain C was the subject of an initial Jack Hills TEM study due to the presence of magnetic zones observed through QDM. This grain appears in the Weiss et al. (2018) study in Fig DR11D. Grain C contained a full range of internal zircon features, including the recovery and recrystallization zones from Grains A and B, but also pristine zircon with no magnetic signal, and fully metamict zones. This grain had not gone through the strict selection criteria for singe crystal paleomagnetism, and was not dated. It was therefore used to characterise the full range of microstructural features typically present in Jack Hills zircons. And also provides evidence the microstructures are not the result of experimental heating during the paleomagnetic experiments undergone by Grains A and B.

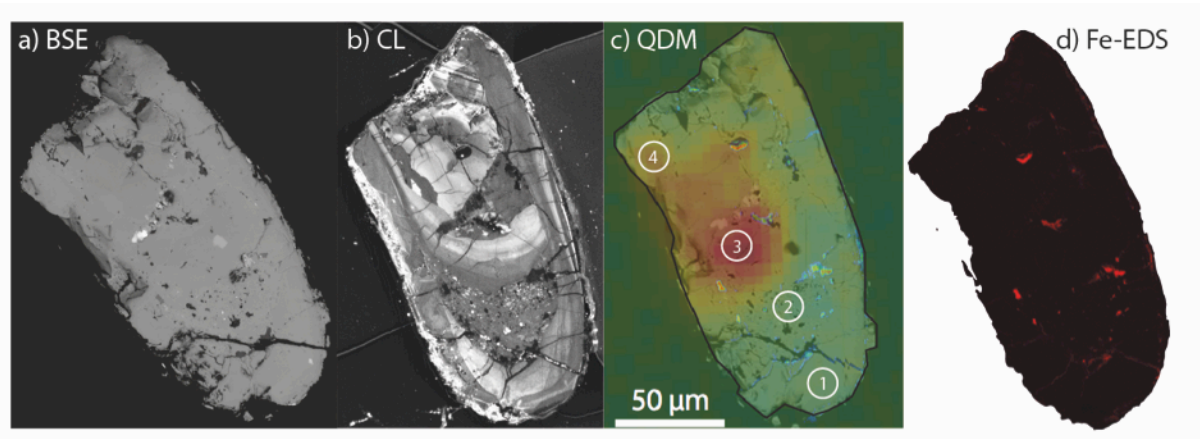

Supplementary Figure S7. SEM and magnetic images of Grain C. Left to right: BSE, CL, QDM, Fe-EDS. QDM images show the locations of target areas of interest for preliminary TEM study. 1) Pristine BSE area with no magnetic signal 2) Metamict zone with high radiation damage and no magnetic signal. 3) Strongly magnetic region. 4) Weakly magnetic region. Apart from the metamict, zone all other regions show a lack of Fe hotspots in the EDS map.

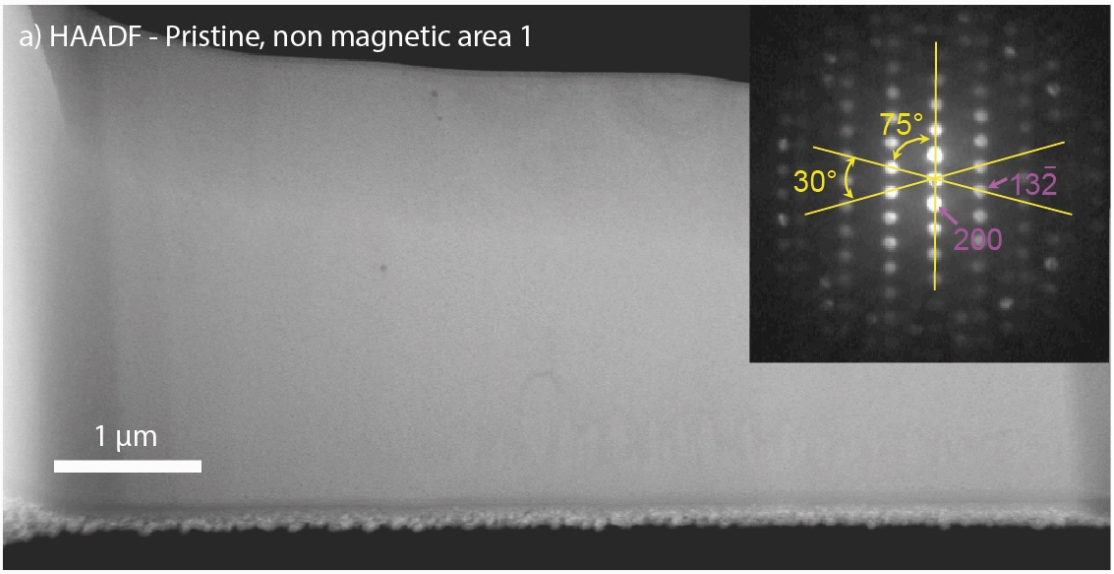

Supplementary Figure S8. HAADF image of TEM foil extracted from Grain C Area 1 – a pristine, non-magnetic area. Inset image shows a cropped TEM diffraction pattern of zircon <0-2-3> zone axis. This sample showed a small number of pores, just visible in the image above and a very low dislocation density. It is difficult to discern whether this sample represents truly pristine original zircon due to lack of zoning – which may be due to the <0-2-3-> orientation – and instead may show a zone that has undergone recrystallization subsequent to a lesser degree of radiation damage than other areas. This sample nevertheless provided a critical test of the sensitivity of the QDM selection method: a lack of QDM signal correlates with an absence of Fe-oxide particles.

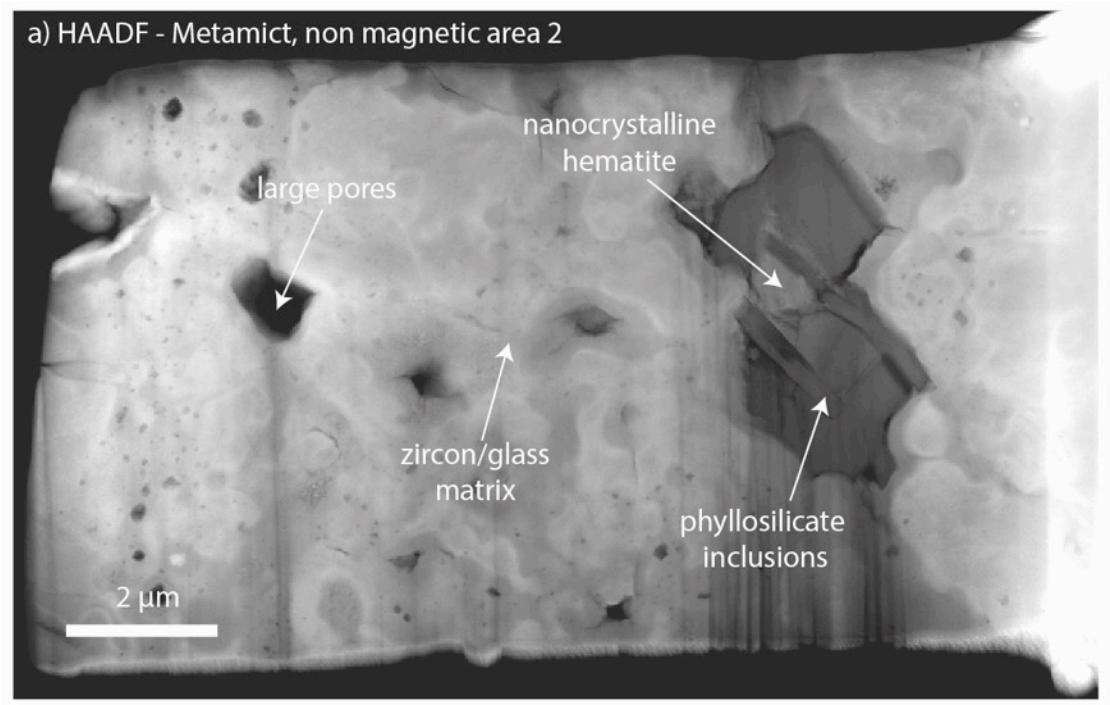

Supplementary Figure S9. HAADF image of TEM foil extracted from Grain C Area 2 – a metamict, non-magnetic area. Matrix comprises a highly heterogeneous mixture of variably radiation-damaged host zircon and secondary inclusions. This results in a complex looking image of variable brightness with a patchy nature, far beyond that seen in the main grains in this study (compared to the more metamict zones in Grain A). Pores appear dark in image and range from tens to hundreds of nm to microns in size. Pore spaces can accommodate a range of secondary inclusions, such as large biotite-chlorite grains that enclose nanocrystalline hematite, a likely source of Fe in the EDS images of metamict zones or micro/nanogranite inclusions. Nanocrystalline structure of hematite, identified through diffraction analysis of TEM sample, is diagnostic of secondary precipitation. No magnetic particles are detected by QDM in this sample or observed in the images.

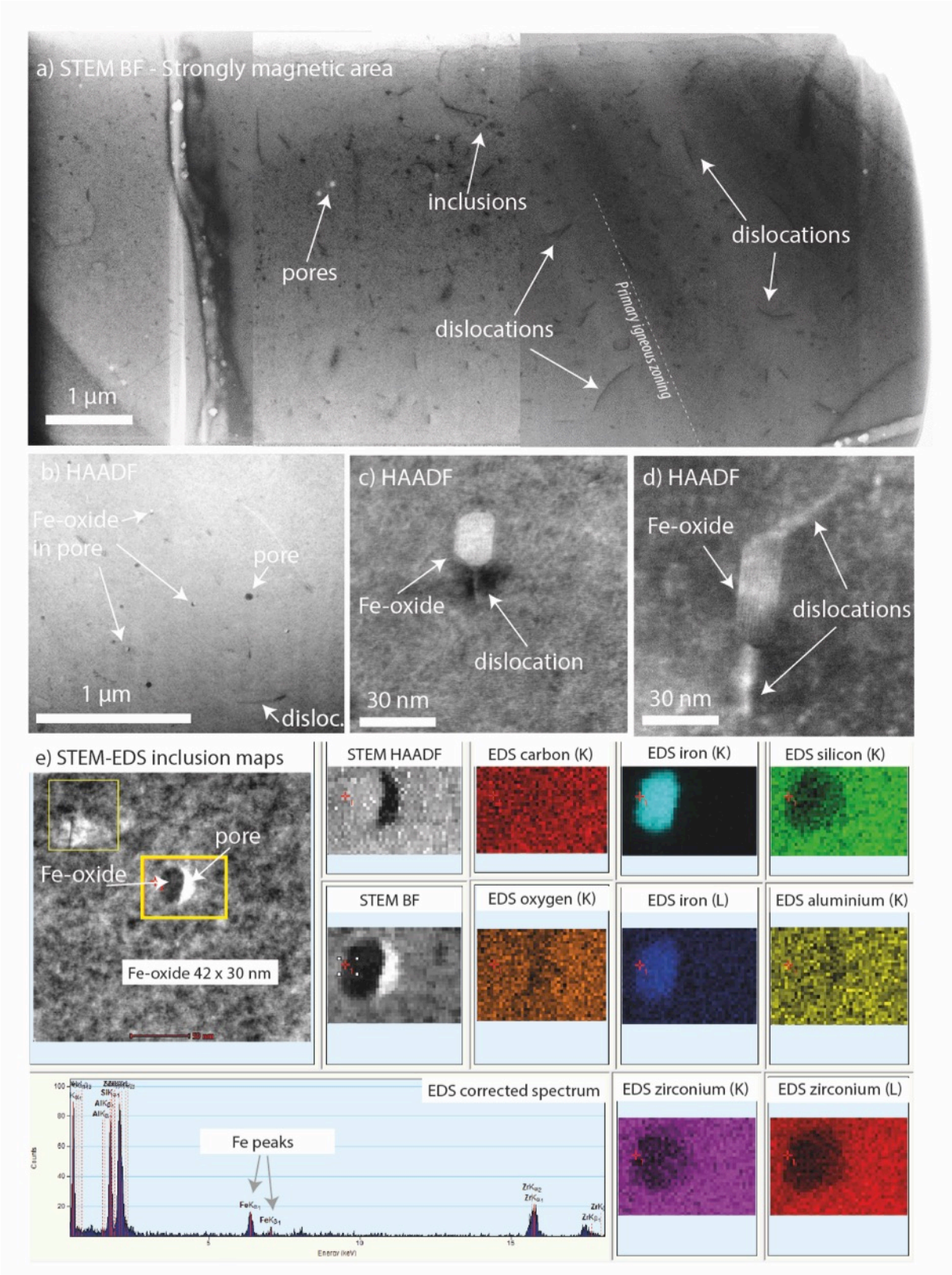

Supplementary Figure S10. STEM images of TEM foil extracted from Grain C Area 3 – a strongly magnetic area. Main article Figure 2f shows an Fe-oxide particle and EDS data from this area. Fracture occupying left of image may also contain secondary magnetic particles, but are not the subject of this study (see Weiss et al., 2018). a) Composite BF image of whole TEM foil showing

microstructures similar to Grain A. Oscillatory zoning is visible, along with pores, filled pores, and dislocations associated with radiation damage recovery. b) Larger scale view demonstrating partially filled pores containing Fe-oxides. c-d) HAADF images of same Fe-oxide particle at different tilt angles. Tilt analysis allows grain dimensions to be accurately calculated, and highlights inclusion position along dislocation feature. e) Example of STEM EDS output showing chemical analysis of inclusions. EDS spectra is mixed analysis of zircon host and Fe-oxide.

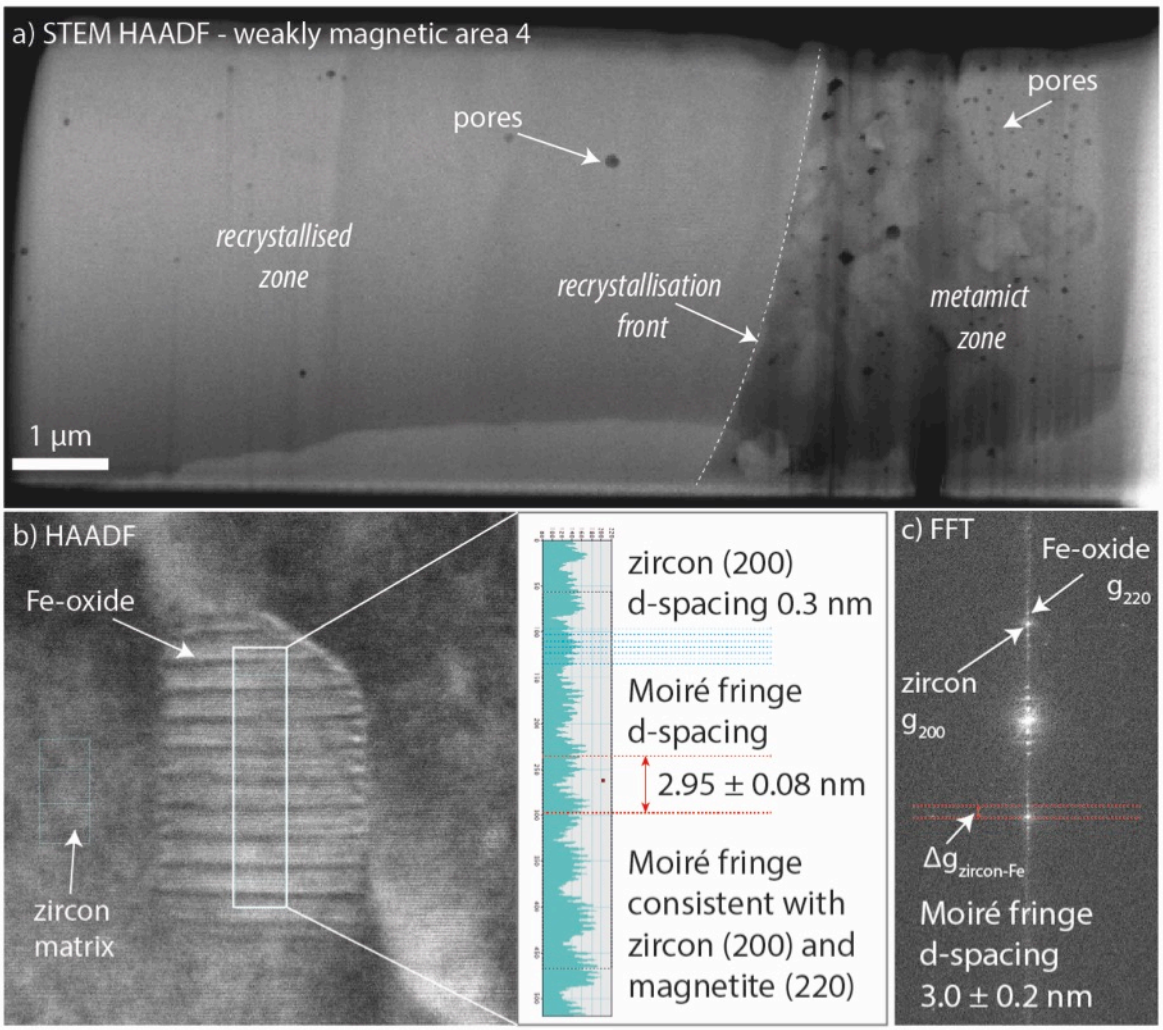

Supplementary Figure S11. STEM images of TEM foil extracted from Grain C Area 4 – a weakly magnetic area. a) HAADF image of whole TEM foil showing microstructures similar to Grain B. Left hand side is predominantly material showing no evidence of primary igneous zonation. Pore spaces are present, and the lack of zonation behind the curved front suggests fluid-assisted recrystallization. Right hand side is a metamict zone/layer with high porosity. Fluid recrystallization front may be advancing into the metamict zone b) Fe-oxide particle from main text Figure 2d. Figure shows calculation of Moiré fringe spacing at ~3 nm superimposed on the zircon (200) lattice plane. Moiré fringe spacing is indicative of magnetite or maghemite (220) lattice plane interference, and is not compatible with hematite. Magnetic data (Supplementary Information C) demonstrates that magnetite

is the Fe-oxide phase present and not maghemite. d) FFT of image data provides another mechanism for measuring Moiré fringe *d*-spacing and confirms zircon-magnetite relationship.

Supplementary information B – Radiation damage model

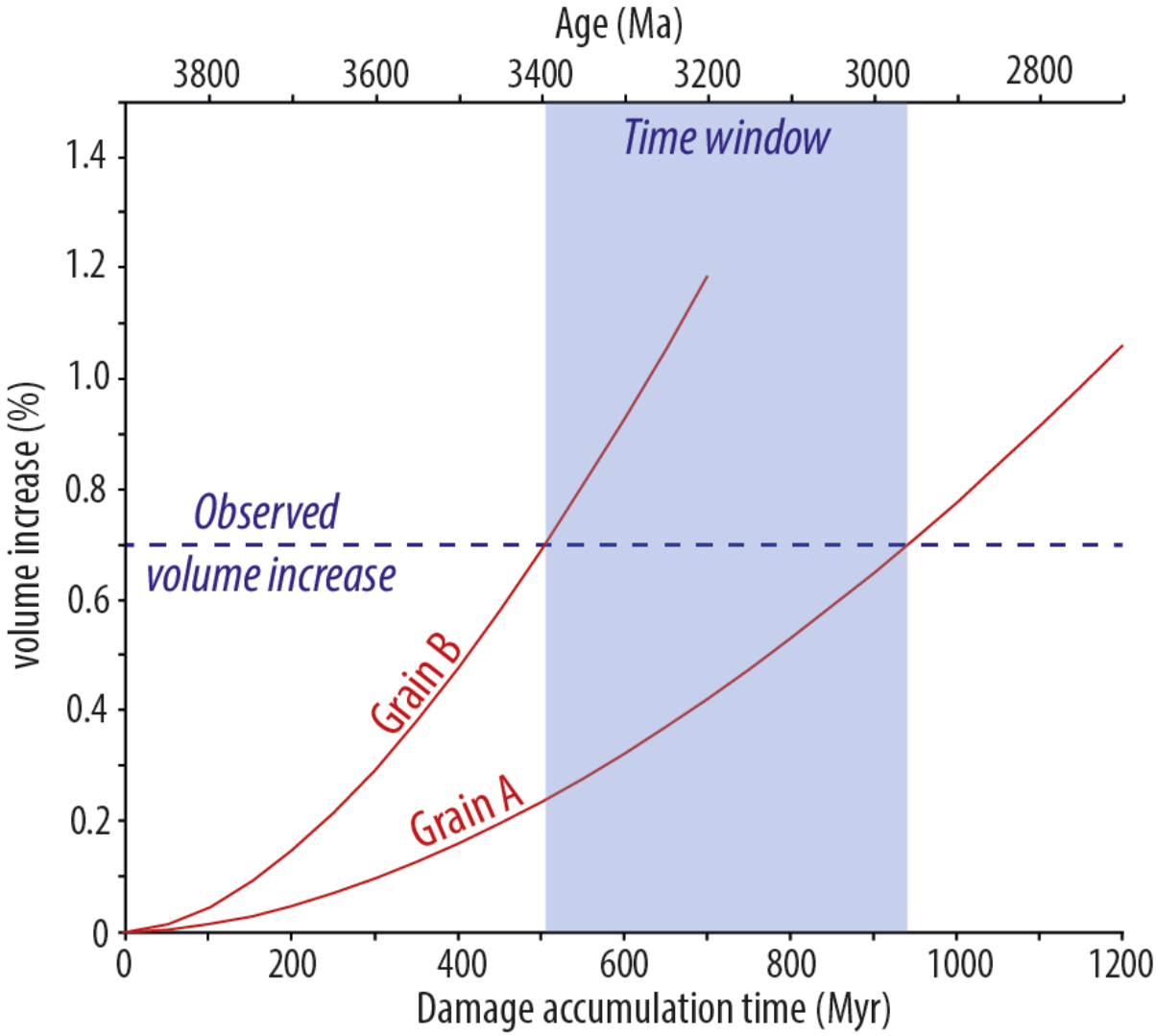

Supplementary Figure S12. Radiation damage model for zircon grains in this study. Image analysis of the porosity in the Jack Hills zircon grains shows approximately 0.7 % increase in the volume of the grain. This volume expansion, caused by the radiation damage associated with U and Th decay is time dependent, and can be converted into time taken to accumulate the damage (Murakami et al., 1991). Red lines show the gradual increase in volume through time for the specific U and Th contents of the two grains, and the time when they cross the observed 0.7 % volume increase. The region of the TEM image for grain A has had original actinide concentrations calculated as 224 ppm U and 171 ppm Th (Th/U = 0.76) and for grain B contained 434 ppm U and 282 ppm Th (Th/U = 0.65). These are typical Th/U ratios for igneous zircon in general (Kirkland et al, 2016). For these concentrations, the time taken to generate a 0.7% volume increase for grains A and B is *c*. 500 and *c*. 950 Myr

respectively, with both grains being *c*. 3900 Ma in age. This value corresponds to less than ~10^{18} alpha decay events, meaning that the level of radiation damage being accommodated at this point is below even the first radiation damage percolation threshold. This timeframe is a lower estimate in the time taken to form the secondary magnetite crystals for several reasons. i) The image analysis did not account for small voids (<10 nm) that are numerous and just visible in the TEM images. ii) We cannot account for pore volumes that have already been accommodated by some level of structural recovery by the formation of dislocations. iii) This only accounts for the formation of space to accommodate the Fe influx, and so magnetite formation can only be determined to be later than the pore formation. Fe-influx and magnetite formation may be due to specific geological events, or a continuous process of influx throughout geological time.

Supplementary information C – Paleomagnetic (demag) data

Measurements of the paleomagnetic data were conducted at the MIT Paleomagnetic Laboratory using the Superconducting Quantum Interference Device (SQUID) microscope (Weiss et al, 2007). Measurements of the magnetic moments of grains A and B followed the protocols from Fu et al, (2017). These data sets are available upon request, and are part of a bigger dataset of paleomagnetic data of the Jack Hills detrital zircon grains to be published in the future.

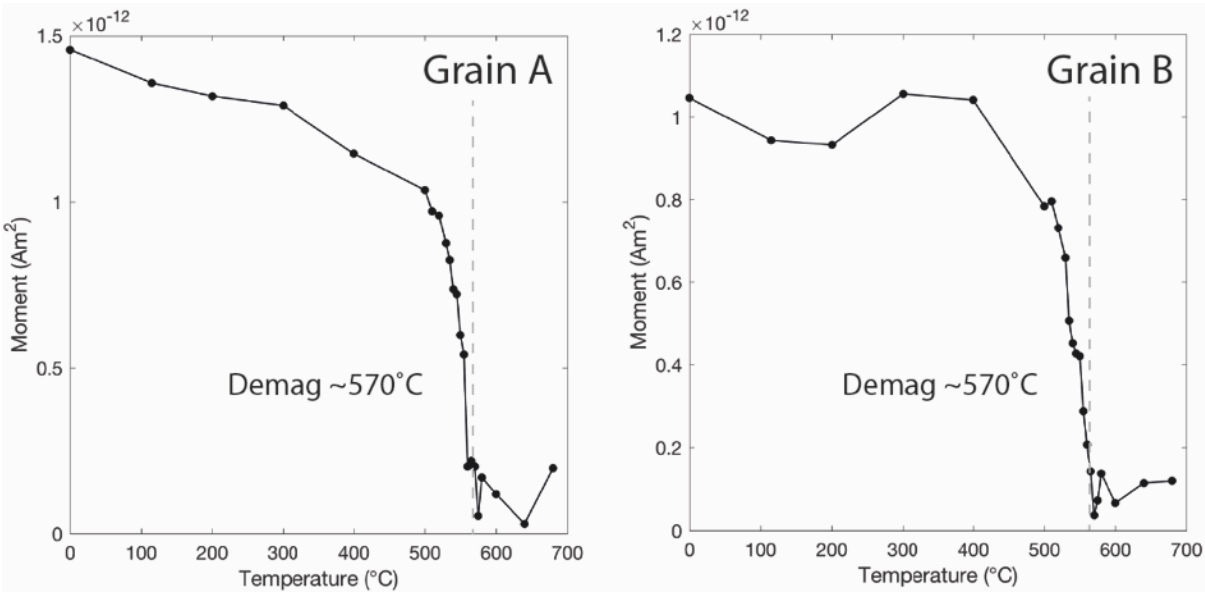

Supplementary Figure S13. Thermal demagnetisation of natural remanent magnetisation of grains A and B, obtained using the scanning SQUID microscopy method of Fu et al. (2017) and Weiss et al. (2018). Rapid demagnetisation occurring in the temperature range 500-570 °C is consistent with the presence of abundant single-domain to vortex-state particles of magnetite observed here with TEM, and with the distribution of blocking temperatures derived from the size and shape of the observed particles using micromagnetic simulations (see Supplementary Information D).

Supplementary Information D – Micromagnetic Modelling

Indicative thermal blocking temperatures (T_B) were calculated using the following assumptions and approximations. Each particle was assumed to be in the single-domain state with uniaxial shape anisotropy. The three-dimensional shape of each particle was approximated as either an ellipsoid of revolution or a square-based prism, as indicated by the labels 'ellipse' and 'rectangular', respectively, in Supplementary Table 1. The aspect ratio of each particle was taken to be L/W. The relationship between T_B and t_{obs} was calculated using the method of Pullaiah et al. (1975):

$$\frac{T_B \ln\left(\frac{t_{obs}}{\tau_0}\right)}{\beta^2(T_B)} = \frac{V M_s(298) H_K(298)}{2k_B} \qquad \text{(Eqn. 1)}$$

where t_{obs} is the observation time, τ_0 is the attempt time, V is particle volume, $M_s(298)$ is the room-temperature saturation magnetisation, $H_K(298)$ is the room-temperature microcoercivity, and k_B is the Boltzmann constant. The β factor defines the temperature dependence of saturation magnetisation:

$$\beta(T) = \frac{M_s(T)}{M_s(298)} = \left(\frac{T_c - T}{T_c - 298}\right)^{0.43} \qquad \text{(Eqn. 2)}$$

where T_c is the Curie temperature. Microcoercivity was calculated assuming shape anisotropy is dominant:

$$H_K(298) = M_s(298)\Delta N \qquad \text{(Eqn. 3)}$$

where ΔN is the difference in demagnetising factor between the short and long axes of the particle. Demagnetising factors were calculated according to Stoner (1945) and Aharoni (1998) for ellipsoids and square-based prisms, respectively. Values of $\tau_0 = 1 \times 10^{-10}$ sec, $M_s(298) = 480$ kA/m, and $T_c = 858$ K were used.

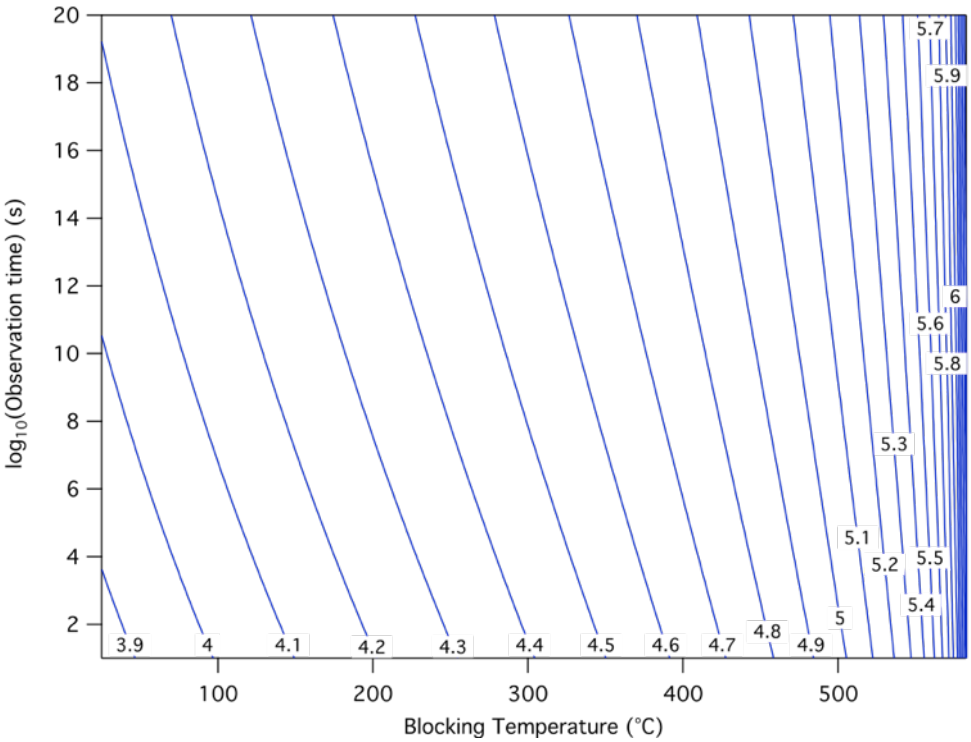

Supplementary Figure S14. Variation of blocking temperature as a function of the observation time for magnetite particles with a given combination of volume and microcoercivity. Contour labels correspond $\log_{10}$ of the right-hand side of Eqn. 1 (referred to as 'stability contour' in Supplementary Table 1). Stability contour values > 5 are required for the preservation of Hadean remanence in the Jack Hills, corresponding to particles that have the potential to retain a primary remanence despite greenschist facies metamorphism of the host rocks to 346-487 °C for ~1-10 Myr (Rasmussen et al., 2010).

Blocking temperatures for the two particles plotting above the single domain to vortex threshold (Fe_#21 and Fe_#32 in Supplementary Table 1; Supplementary Figure 4e and Supplementary Figure 5d) were calculated using micromagnetic simulations according to the method of Nagy et al. (2017). Calculations were performed using the MERRILL finite-element code (Conbhuí et al.). The grain geometries were defined using linear tetrahedral elements with an average edge length of 8nm (c.f. the exchange length for magnetite of 9nm). Energy barriers were calculated using the nudged elastic band (NEB)/ minimum action method of Fabian and Shcherbakov (2017). Particle Fe_#21 was approximated as an elongated octahedron with minor truncations to create small {001} type faces at the apices of the octahedron (Supplementary Movie S15). Particle Fe_#32 was modelled as an ellipsoid of revolution (Supplementary Movie S16). Particle Fe_#21 adopts a uniformly magnetised remanence state, with easy axis aligned with elongation direction of the octahedron. Particle Fe_#32 is a single-vortex state at remanence, with vortex core aligned with the elongation direction of the

ellipsoid. In both cases, the magnetisation reversal mechanism involves the formation and rotation of a single-vortex state, with the vortex core being forced to rotate across the short-axis of the particle. This traverse of the short axis by the vortex core results in a large energy barrier for magnetisation reversal, and a correspondingly high blocking temperature (T_B = 570 °C for Fe_#21 and T_B = 575 °C for Fe_#32, assuming 100 sec laboratory observation times). These values are close to those obtained using the single-domain approximation ($T_B = T_c$ = 585 °C for Fe_#21 and T_B = 582 °C for Fe_#32; Supplementary Table 1), although single-domain theory clearly misrepresents the reversal mechanism and exact nature of the domain states. In order to isolate putative primary Hadean paleomagnetism, thermal demagnetisation to a temperature of 565 °C is used (Tarduno et al., 2015). These simulations demonstrate, however, that such a procedure is not capable of removing the younger secondary component of CRM carried by magnetite particles formed during recrystallisation and recovery.

Movie Legends

Movie S15. Micromagnetic simulation of magnetic reversal in particle #21 (elongated tetrahedron) showing formation and rotation of single domain vortex state. Modelling determines a large energy barrier for magnetic reversal as the vortex core is forced to rotate across the short axis of the particle. Upper panel) Three grain orientations showing orientation of vortex core only. Lower panel) Three grain orientations showing full micromagnetic simulation.

Movie S16. Micromagnetic simulation of magnetic reversal in particle #32 (ellipsoid of revolution) showing formation and rotation of single domain vortex state. As with the previous example, modelling determines a large energy barrier for magnetic reversal as the vortex core is forced to rotate across the short axis of the particle. Upper panel) Three grain orientations showing orientation of vortex core only. Lower panel) Three grain orientations showing full micromagnetic simulation.

Supplementary Information E – Uranium-Lead dating

Zircon grains were analysed during U-Pb sessions on the Cameca IMS 1270 Ion Microprobe at UCLA during sessions on 9/5/2017 (Grain A) and 7/7/2016 (Grain B). The instrument was operated under standard procedures for the collection of U and Pb isotopes. U-Pb isotopic measurements were calibrated against multiple analyses of standard reference material AS3 (Paces and Miller, 1993) throughout the analytical sessions.

Isotopic data for the 2 grains in this study are in the table below. This includes ages and isotopic ratios for $^{206}Pb/^{238}U$, $^{207}Pb/^{235}U$ and $^{207}Pb/^{206}Pb$ along with calculated 1 s.e. uncertainties. Values of concordance have also been calculated in terms of deviation of the datapoint centroid from the concordia curve for Pb-Pb (defined as % difference of $^{206}Pb/^{238}U$ and $^{207}Pb/^{206}Pb$ ages) and U-Pb

(defined as % difference of $^{206}Pb/^{238}U$ and $^{207}Pb/^{206}Pb$ ages) with a maximum value of 4%. Both analyses fit a true definition of concordance in that the 2 sigma error ellipse overlaps the concordia curve (Spencer et al, 2016). Common Pb corrections (based on measured ^{204}Pb) are minor with a calculated radiogenic Pb component of ~99.9% in both grains. Data table and Tera-Wasserburg concordia plot are shown below. Grain A in Blue, Grain B in Red.

Name	**Cambridge**	*manuscript*		**Grain A**	**Grain B**
Name	**MIT**	*paleomag*		**080211_h30**	**071320_h02**
Name	**UCLA**	*UPb*		**UCLA 8_2_11.ais**	**UCLA 7_13_20.ais**
Age (Ma)	206Pb/	238U		3990	3899
error (Ma)	*206Pb/*	*238U*	*1 s.e.*	*297*	*121*
Age (Ma)	207Pb/	235U		3983	3948
error (Ma)	*207Pb/*	*235U*	*1 s.e.*	*100*	*41*
Age (Ma)	207Pb/	206Pb		3979	3973
error (Ma)	*207Pb/*	*206Pb*	*1 s.e.*	*7*	*1*
Concordance	Pb-Pb		%	0	2
	U-Pb		%	0	1
Ratio	207Pb*/	235U		49.52	47.80
error	*207Pb*/*	*235U*	*1 s.e.*	*4.96*	*1.98*
Ratio	206Pb*/	238U		0.86	0.83
error	*206Pb*/*	*238U*	*1 s.e.*	*0.09*	*0.03*
Correlation of concordia ellipses				1.00	1.00
Ratio	238U/	206Pb*		1.17	1.20
error	*238U/*	*206Pb**	*1 s.e.*	*0.12*	*0.01*
Ratio	207Pb*/	206Pb*		0.42	0.42
error	*207Pb*/*	*206Pb**	*1 s.e.*	*0.002*	*0.0003*
Common	206Pb/	204Pb		18.86	18.86
Common	207Pb/	204Pb		15.62	15.62
Common	208Pb/	204Pb		38.34	38.34
Pb corr.				(204Pb)	(204Pb)
% Radiogenic	206Pb			99.89	99.95

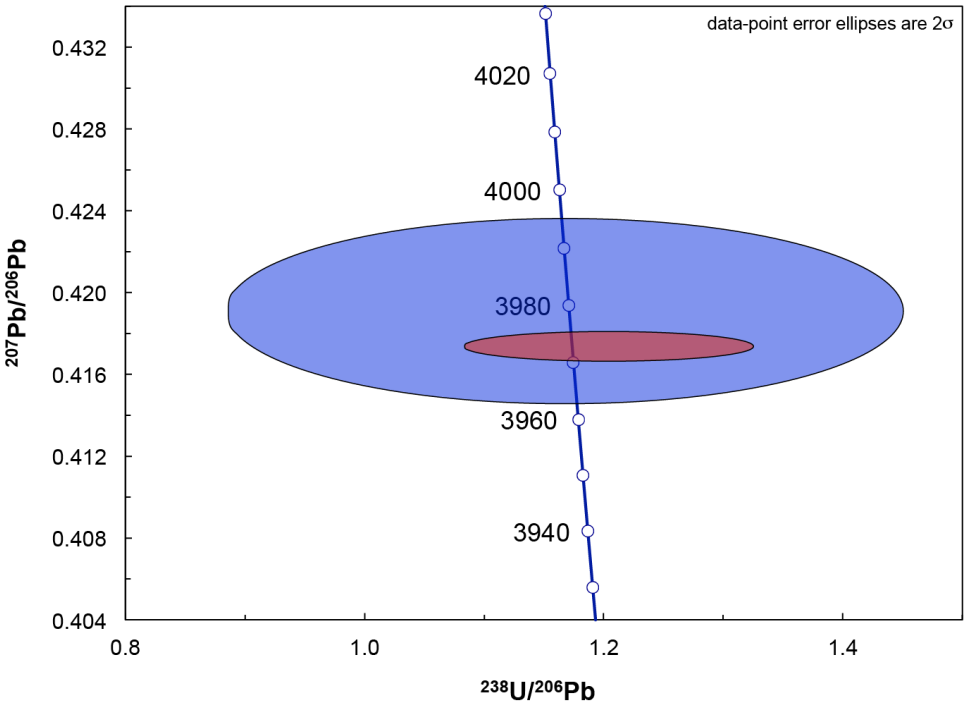

Supplementary Figure S15. Inverse concordia plot showing isotopic data for grains in this study.

Supplementary References

Aharoni, A., 1998. Demagnetizing factors for rectangular ferromagnetic prisms. Journal of applied physics, 83(6): 3432-3434.

Conbhuí, P.Ó. et al., MERRILL: Micromagnetic Earth Related Robust Interpreted Language Laboratory. Geochemistry, Geophysics, Geosystems.

Fabian, K., Shcherbakov, V.P., 2017. Energy barriers in three-dimensional micromagnetic models and the physics of thermo-viscous magnetization in multidomain particles. arXiv preprint arXiv:1702.00070.

Fu, R.R. et al., 2017. Evaluating the paleomagnetic potential of single zircon crystals using the Bishop Tuff. Earth and Planetary Science Letters, 458: 1-13.

Kirkland, C.L., et al., 2015. Zircon Th/U ratios in magmatic environs. *Lithos*, *212*, pp.397-414.

Murakami, T., Chakoumakos, B.C., Ewing, R.C., Lumpkin, G.R., Weber, W.J., 1991. Alpha-decay event damage in zircon. American Mineralogist;(United States), 76.

Muxworthy, A.R., Williams, W., 2008. Critical superparamagnetic/single-domain grain sizes in interacting magnetite particles: implications for magnetosome crystals. Journal of the Royal Society Interface: rsif. 2008.0462.

Nagy, L. et al., 2017. Stability of equidimensional pseudo–single-domain magnetite over billion-year timescales. Proceedings of the National Academy of Sciences, 114(39): 10356-10360.

Paces, J.B. and Miller Jr, J.D., 1993. Precise U-Pb ages of Duluth complex and related mafic intrusions, northeastern Minnesota: Geochronological insights to physical, petrogenetic, paleomagnetic, and tectonomagmatic processes associated with the 1.1 Ga midcontinent rift system. *Journal of Geophysical Research: Solid Earth*, *98*(B8), pp.13997-14013.

Pullaiah, G., Irving, E., Buchan, K., Dunlop, D., 1975. Magnetization changes caused by burial and uplift. Earth and Planetary Science Letters, 28(2): 133-143.

Rasmussen, B., Fletcher, I.R., Muhling, J.R., Wilde, S.A., 2010. In situ U-Th-Pb geochronology of monazite and xenotime from the Jack Hills belt: Implications for the age of deposition and metamorphism of Hadean zircons. Precambrian Research, 180(1-2): 26-46.

Spencer, C.J., Kirkland, C.L. and Taylor, R.J., 2016. Strategies towards statistically robust interpretations of in situ U–Pb zircon geochronology. *Geoscience Frontiers*, *7*(4), pp.581-589.

Stoner, E.C., 1945. XCVII. The demagnetizing factors for ellipsoids. The London, Edinburgh, and Dublin philosophical magazine and journal of science, 36(263): 803-821.

Tarduno, J.A., Cottrell, R.D., Davis, W.J., Nimmo, F., Bono, R.K., 2015. A Hadean to Paleoarchean geodynamo recorded by single zircon crystals. Science, 349(6247): 521-524.

Weiss, B.P. et al., 2018. Secondary magnetic inclusions in detrital zircons from the Jack Hills, Western Australia, and implications for the origin of the geodynamo. Geology.

Supplementary Table 1

Grain A	Ref.	L (nm)	Error	W (nm)	Error	Ratio (L/W)	Error	Approx. Shape	Location	Stability Contour	TB°C [100 sec]
Box 1	Fe_#1	122	3	21	2	5.8	0.6	Rectangular		5.34	549
	Fe_#2	43	3	20	2	2.2	0.3	Rectangular	Pore	4.60	384
	Fe_#3	63	4	45	3	1.4	0.1	Rectangular	Dislocation	5.15	528
	Fe_#4	39	3	12	3	3.3	0.9	Rectangular		4.25	221
	Fe_#5	59	4	33	4	1.8	0.2	Rectangular	Pore	5.07	515
	Fe_#6	46	3	17	3	2.7	0.5	Rectangular	Dislocation	4.57	375
Box 2	Fe_#7	81	4	36	3	2.3	0.2	Rectangular	Pore	5.40	554
	Fe_#8	38	3	12	3	3.2	0.8	Rectangular		4.23	212
	Fe_#9	37	3	9	2	4.1	1.0	Rectangular	Dislocation	4.03	104
	Fe_#10	33	4	15	3	2.2	0.5	Rectangular		4.24	216
	Fe_#11	30	3	11	2	2.7	0.6	Rectangular	Dislocation	4.01	95
	Fe_#12	42	4	40	3	1.1	0.1	Rectangular	Pore	4.06	117
	Fe_#13	31	4	17	3	1.8	0.4	Rectangular		4.23	207
	Fe_#14	59	3	21	2	2.8	0.3	Rectangular	Dislocation	4.88	475
	Fe_#15	52	4	37	3	1.4	0.2	Rectangular	Pore	4.90	481
Box 3	Fe_#1 6	68	3	9	2	7.6	1.7	Rectangular	Pore	4.37	283
	Fe_#17	55	5	47	5	1.2	0.2	Ellipse	Pore and dislocation	4.61	389
	Fe_#18	45	3	44	3	1.0	0.1	Ellipse		3.63	SP
	Fe_#19	50	2	8	2	6.3	1.6	Rectangular	Dislocation	4.12	150
	Fe_#20	56	2	12	2	4.7	0.8	Rectangular		4.48	334

Grain B	Ref.	L (nm)	Error	W (nm)	Error	L/W	Error	Approx. Shape	Location	Stability Contour	TB°C [100 sec]
Recovery zone	Fe_#21	200	4	118	3	1.69	0.05	Ellipse	Pore	6.46	585
	Fe_#22	130	4	110	3	1.18	0.05	Ellipse	Pore and dislocation	5.75	572
	Fe_#23	70	3	46	3	1.52	0.12	Ellipse		5.10	520
	Fe_#24	68	3	47	3	1.45	0.11	Ellipse	Dislocation	5.06	513
	Fe_#25	35	3	30	3	1.17	0.15	Ellipse		4.02	98
	Fe_#26	50	4	40	3	1.25	0.14	Ellipse		4.58	377
	Fe_#27	65	4	57	4	1.14	0.11	Ellipse	Pore	4.78	447
	Fe_#28	70	4	50	3	1.40	0.12	Rectangle	Pore	5.29	544
	Fe_#29	53	3	29	3	1.83	0.22	Rectangle	Pore	4.92	485
	Fe_#30	80	3	51	3	1.57	0.11	Ellipse	Pore	5.28	543
Recrystallized zone	Fe_#31	26	3	18	3	1.44	0.29	Ellipse		3.80	SP
	Fe_#32	184	7	87	5	2.11	0.15	Ellipse	Dislocation	6.29	582
	Fe_#33	13	3	9	2	1.44	0.46	Ellipse	Inclusion in ZrO2	2.90	SP
	Fe_#34	54	3	25	3	2.16	0.29	Rectangle	Dislocation	4.89	477
	Fe_#35	24	3	22	2	1.09	0.17	Ellipse	Dislocation	3.34	SP
Metamic zone	Fe_#36	28	3	25	3	1.12	0.18	Ellipse	Pore	3.63	SP
	Fe_#37	48	3	30	3	1.60	0.19	Ellipse	Pore	4.61	389
	Fe_#38	40	3	35	3	1.14	0.13	Ellipse	Dislocation	4.15	167
	Fe_#39	44	3	27	3	1.63	0.21	Ellipse	Pore	4.50	342
	Fe_#40	45	3	31	3	1.45	0.17	Ellipse	Pore	4.52	351

Grain C Lamella 1	Ref.	L (nm)	Error	W (nm)	Error	L/W	Error	Approx. Shape	Location	Stability Contour	TB°C [100 sec]
Recrystallized zone	Fe_#41	20	2	14	2	1.43	0.25	Rectangular	Dislocation	3.66	SP
	Fe_#42	32	2	20	2	1.60	0.19	Rectangular	Dislocation	4.29	239
	Fe_#43	21	2	16	2	1.31	0.21	Rectangular		3.69	SP
	Fe_#44	29	2	13	2	2.23	0.38	Rectangular	Dislocation	4.07	124

Grain C Lamella 2	Ref.	L (nm)	Error	W (nm)	Error	L/W	Error	Approx. Shape	Location	Stability Contour	TB°C [100 sec]
Recrystallized zone	Fe_#145	32	2	20	2	1.60	0.19	Rectangular	Pore	4.29	239
	Fe_#46	25	2	22	2	1.14	0.14	Ellipse	Pore	3.52	SP
	Fe_#47	50	2	17	2	2.94	0.37	Rectangular	Dislocation	4.64	399
	Fe_#48	25	2	12	2	2.08	0.39	Ellipse	Pore	3.70	SP
	Fe_#49	26	2	12	2	2.17	0.40	Rectangular	Dislocation	3.94	57
	Fe_#50	35	2	9	2	3.89	0.89	Rectangular	Dislocation	4.00	86
	Fe_#51	22	2	21	2	1.05	0.14	Ellipse	Pore	3.00	SP
	Fe_#52	26	2	23	2	1.13	0.13	Ellipse	Pore	3.56	SP
	Fe_#53	46	2	20	2	2.30	0.25	Rectangular	Pore	4.66	406
	Fe_#54	22	2	15	2	1.47	0.24	Rectangular	Dislocation	3.79	SP
	Fe_#55	30	2	22	2	1.36	0.15	Rectangular	Pore and dislocati	4.18	180

Grain C Lamella 3	Ref.	L (nm)	Error	W (nm)	Error	L/W	Error	Approx. Shape	Location	Stability Contour	TB°C [100 sec]
Recrystallized zone	Fe_#56	63	2	27	2	2.33	0.188	Rectangular		5.06	513